Publisher: GSA
Journal: GEOL: Geology
DOI:10.1130/G38671.1

Tracing weathering regimes using the lithium isotope composition of detrital sediments

Mathieu Dellinger[1,2], Julien Bouchez[2], Jérôme Gaillardet[2], Laetitia Faure[2], and Julien Moureau[2]

[1]*Geography Department, Durham University, South Road, Durham, DH1 3LE, United Kingdom*

[2]*Institut de Physique du Globe de Paris, Sorbonne Paris Cité, University Paris Diderot, CNRS, Paris, France*

ABSTRACT

Lithium (Li) isotopes are a promising tracer of chemical weathering processes for both modern and ancient times. In order to improve the use of Li isotopes in the sedimentary record, here we calibrate the relationship between weathering intensity and detrital Li isotope composition (δ^7Li) using the fine fraction of modern large river sediments. By using independent estimates for sediment provenance to calculate the Li isotope signature of the rock from which the sediments derive through weathering, we show that source rock variability (in particular the relative contribution of sedimentary *vs.* igneous rocks) must be corrected for before using Li isotopes as a weathering proxy. We also show that for rivers draining mountain ranges, the contribution of particles derived from sedimentary rocks to river sediments is correlated to their Li/Al ratio, making it possible to use Li contents to estimate the average source rock composition. Once corrected for bedrock variability, the Li isotope signature defines a negative relationship with the weathering intensity (ratio between silicate weathering rate and total denudation

Publisher: GSA
Journal: GEOL: Geology
DOI:10.1130/G38671.1

rate) with highest Li isotope fractionation for the highest weathering intensity. Altogether, we propose a set of new relationships between weathering, erosion, provenance and Li isotopes that can be used to quantify present-day and paleo-weathering using detrital sediment.

INTRODUCTION

The surface of Earth evolves through the combined action of chemical weathering reactions and physical denudation. The former process partly dissolves the continental crust, exports cations to the ocean, and consumes atmospheric CO_2 from the atmosphere, whereas physical denudation exports solid products to the ocean. Hence, over long time scales, silicate weathering is one of the major processes regulating the amount of atmospheric CO_2 and therefore controlling the evolution of climate (Berner et al., 1983). Despite this recognition, it is still poorly known how silicate weathering has changed in the past and what are the parameters controlling weathering rates and intensities over long timescales. The emerging Li isotope proxy has a great potential for tracing silicate weathering because Li is a soluble element predominantly hosted in silicate rocks and its isotopes are fractionated during water-rock interactions (Huh et al., 2001). Although the relation between the river dissolved Li isotope composition (δ^7Li) and weathering is still a matter of debate (e.g., Dellinger et al., 2015; Huh et al., 2001; Pogge von Strandmann and Henderson, 2015), this has served as a basis to investigate the δ^7Li of ancient marine carbonates (e.g., Misra and Froelich, 2012; Pogge von Strandmann et al., 2013) in order to unravel global past weathering conditions (Bouchez et al., 2013; Li and West, 2014; Misra and Froelich, 2012).

Publisher: GSA
Journal: GEOL: Geology
DOI:10.1130/G38671.1

Complementary to this approach, the characterization of weathering conditions with Li isotopes can also be achieved with the study of detrital sediments. However, several difficulties arise for using sediments δ^7Li to trace weathering and erosion in modern systems. First, detrital sediments not only contain weathered products but also unweathered minerals deriving from the physical erosion of the bedrock (Dellinger et al., 2014). Secondly, the δ^7Li of river sediments is quite variable depending on the sediment grain size (Dellinger et al., 2014). Finally, as on average 80% of the total Li in the weathering system is contained in the solid load and only 20% in the dissolved load (Misra and Froelich, 2012), terrigenous sediment δ^7Li is usually close to that of source rock (Bouchez et al., 2013), such that the source rock δ^7Li has a large imprint on the composition of the detrital material (Dellinger et al., 2014). In this contribution, we use the available data from the literature to investigate how the δ^7Li of medium to large river-sediments relates to the present-day weathering regimes.

PRESENT-DAY RIVER SEDIMENTS DATASET

The data set used in this study includes some of the largest Earth river systems: the Amazon, Mackenzie, Ganges and Brahmaputra (Dellinger et al., 2015, 2014), Congo (Henchiri et al., 2016) and Changjiang (also known as the Yangtze River; Wang et al., 2015). It is complemented by new data from the Stikine and Skeena River from the western Canadian cordillera, two large rivers draining predominantly volcanic rocks (Gaillardet et al., 2003). All these rivers drain a surface larger than 19,000 km^2, and cover a wide range of lithology, climate, and weathering regimes such that this data set can be considered as globally representative. In the following, we characterize the modern weathering regimes by using the weathering intensity parameter "(W/D)", which is

Publisher: GSA
Journal: GEOL: Geology
DOI:10.1130/G38671.1

independent of the drainage area and the discharge, and defined as the ratio between chemical silicate weathering rates W (calculated as the flux of river dissolved material sourced from silicate rocks only) and total denudation rate D, thereby corresponding to the proportion of weathering material transported in the dissolved form by the river.

Within the set of rivers from this study, we distinguish two groups: (1) rivers draining high elevation mountain ranges (the Andes, Himalayas, Western Canadian Cordillera) characterized by moderate to high erosion rates (>100 t km^{-2} yr^{-1}), low weathering intensity (W/D < 0.1), and a kinetically limited weathering regime (West et al., 2005); and (2) rivers draining lowlands with deep weathered soils, low erosion rates, and high weathering intensity (W/D > 0.1) corresponding to the supply-limited weathering regime (West et al., 2005).

Overall, for rivers draining mountain ranges, the Li concentration of river sediments ranges from 10 to 102 μg g^{-1} (ppm) and the δ^7Li of the sediments ($\delta^7Li_{suspended\_load}$, precision better than ‰) from –4‰ to +5‰ (Fig. 1). The rivers draining lowlands have on average lower δ^7Li (–6.5‰ to –3‰) and Li concentration compared to rivers draining mountain ranges. Interestingly, the δ^7Li is negatively correlated to the Li concentrations in large rivers draining mountain ranges, whereas no relationship is observed for rivers draining the lowlands (Fig. 1).

REMOVING THE NON-WEATHERING EFFECTS

In large rivers draining mountain ranges, the δ^7Li and Li concentration of river sediments are strongly dependent upon grain size and lithological source (Dellinger et al., 2014). In order to extract the weathering signal contained in river sediments, it is

Publisher: GSA
Journal: GEOL: Geology
DOI:10.1130/G38671.1

necessary to remove the effect of both grain size and lithological variability on the Li isotope composition.

Grain Size Effects

Fine sediments have generally lower δ^7Li and higher Li concentration than coarse sediments (Fig. 1). This is because they contain a higher proportion of particles sourced from sedimentary rocks and a higher proportion of weathering products sourced from modern soils that carry the fingerprint of the modern weathering regime (Dellinger et al., 2014). Therefore, similarly to element ratios (e.g., Lupker et al., 2013), large changes of the δ^7Li in sedimentary archives can simply arise from change of the sediment grain size and lead to false interpretation in terms of shift in weathering conditions. In order to mitigate this grain size effect, in the present study we use for each river the finest sediment sample available (size < 63 μm), which for most cases has been collected at or near the river channel surface. However, even these fine sediments contain a non-negligible fraction of unweathered material that needs to be taken into account for the interpretation of their δ^7Li data.

The Influence of Lithology

The Li isotope signature that can be measured in weathered detrital material depends upon (1) the initial δ^7Li of river sediments, prior to chemical weathering (i.e., the Li isotope signature of its source rock material, hereafter referred to as "$\delta^7Li_{source\_material}$"), which is a lithological effect and (2) the extent of fractionation between this initial signature and the neoformed weathering material, which in turn depends on isotope fractionation factors and on Li partitioning between secondary minerals and the dissolved load (Bouchez et al., 2013). The weathering signal is contained only in the second effect.

Publisher: GSA
Journal: GEOL: Geology
DOI:10.1130/G38671.1

This is why in the following, we consider the difference in isotope composition between the fine suspended sediment and the original bedrock, $\Delta^7Li_{fine\text{-}source} = \delta^7Li_{fine\ suspended\_load} - \delta^7Li_{source\_material}$.

The "$\delta^7Li_{source\_material}$" corresponds to the weighted average of the δ^7Li of the various erosion sources: igneous, metamorphic and sedimentary rocks (hereafter referred to as "shale" because shales are by far the most important type of sedimentary rock contributing to the Li budget; Holland, 1984) that have distinct average Li concentration and isotope composition (Dellinger et al., 2014; Sauzéat et al., 2015; Tomascak et al., 2016). Indeed, the Li isotope variability of the present-day upper continental crust (UCC), as characterized by using inherently integrative samples like large river sand (Dellinger et al., 2014) or desert loess (Sauzéat et al., 2015), corresponds mostly to a mixture between a Li-rich, low-δ^7Li, shale end member (δ^7Li of -0.5 ± 1‰ and Li/Al of $1.0 \pm 0.1 \times 10^{-3}$) and a Li-poor, high-$\delta^7Li$, igneous end member ($\delta^7Li$ of 3.5 ± 1.5‰, Li/Al of $0.30 \pm 0.12 \times 10^{-3}$). This mixing trend can be used to determine the Li isotope composition of river sediments prior to weathering ($\delta^7Li_{source\_material}$) provided that the relative contribution of the different source materials to the sediments is known.

Quantification of the provenance of sediments can be achieved using Sr-Nd isotopes and/or insoluble trace element ratios, provided that the composition of the major bedrock drained by each river basin is known and that they have contrasted signatures (e.g., Allègre et al., 1996). Here, we use independent tracers of provenance (Nd, Sr isotopes and trace elements) in order to quantify the erosion sources of the fine sediments and determine the $\delta^7Li_{source\_material}$ for fine sediments from each of the large rivers. We note that the procedure of choice to characterize average source rock is specific to each

Publisher: GSA
Journal: GEOL: Geology
DOI:10.1130/G38671.1

large river basin. In the Amazon, Congo, and Ganges-Brahmaputra basins, sedimentary, igneous, and metamorphic rocks have distinct Nd isotope composition making it possible to quantify precisely the provenance of fine sediments using Nd isotopes (see the GSA Data Repository[1]). For the Mackenzie River, we use trace elements (Cr, Ti, Cs) ratios (see the Data Repository). We emphasize that this calculation provides information on source rocks for fine sediments only, which can be different for other grain sizes (Bouchez et al., 2011a; Dellinger et al., 2014; Garçon and Chauvel, 2014).

However, in some cases like that of the Changjiang basin, neither Sr-Nd isotopes nor trace elements can be used to assess the provenance of sediments because the signatures of the main rock sources are under-constrained or not significantly different (Chetelat et al., 2013). An alternative method is to identify another tracer that correlates with an independent measure of the proportion of shale-derived particles (i.e., the amount of sedimentary recycling) quantified across the rest of our river set. Among all the chemical elements tested, the best correlation with the proportion of shale-derived particles is obtained for the Li/Al ratio (Fig. 2). Li concentrations are normalized to Al to remove dilution effect by quartz or other Li-free phases. This good relationship stems mostly from the fact that (1) shales and igneous rocks have significantly distinct Li contents, and (2) that chemical weathering has a minor impact on sediment Li content for a majority of samples. However, we note that sediments from some lowland rivers have lost a significant fraction of Li because of their higher weathering intensity (Fig. 3). Using the relationship between Li and the proportion of sediments derived from erosion of shales calibrated on rivers draining mountain ranges, we infer the proportion of shales

Publisher: GSA
Journal: GEOL: Geology
DOI:10.1130/G38671.1

contributing to the fine sediment load of the Changjiang basin river, which makes our set of $\delta^7Li_{source\_material}$ estimates complete (see Data Repository).

Using the calculated proportion of shales and igneous rocks with the δ^7Li of the rock end members, we estimate the Li isotope composition of the rock source ($\delta^7Li_{source\_material}$) for each fine river sediment sample (see the Data Repository). We note that the calibration of the Li provenance tracer in detrital sediments might also serve to determine the provenance and the $\delta^7Li_{source\_material}$ of ancient detrital sedimentary archives for which the potential bedrock sources are usually not constrained.

RELATION BETWEEN THE LITHIUM ISOTOPE SIGNATURE AND WEATHERING INTENSITY

In this section we evaluate the relation between sediment δ^7Li, Li weathering index and the weathering intensity previously defined as the W/D ratio. The Li weathering index of the detrital sediment can be expressed as $(Li/Al)_{fine\_sediments}$ / $(Li/Al)_{source\_material}$, where $(Li/Al)_{source\_material}$ corresponds here to the (Li/Al) ratio the suspended sediments would have in the absence of any silicate weathering reactions. A value of 1 means no loss or gain of Li by the solids during weathering while a value lower than 1 implies loss of Li during weathering. The "$(Li/Al)_{source\_material}$" values are determined using the rock end member compositions defined in the previous section and the proportion of shales calculated above. The Li weathering index values are negatively correlated to the weathering intensity (Fig. 2.b) with most of the rivers draining mountain ranges having a Li weathering index higher than 0.8 (except for the Solimões and Pastaza rivers), whereas rivers draining lowlands have Li weathering index values between 0.9 and 0.4. The higher Li depletion in sediments transported by lowland rivers is compatible

Publisher: GSA
Journal: GEOL: Geology
DOI:10.1130/G38671.1

with the higher proportion of dissolved Li transported by these rivers (see the Data Repository). This shows that significant Li depletion in sediments occurs only for very intense weathering conditions (Fig. 2).

The relationships between Li isotope signature in modern fine river sediments corrected for the source rock signature ($\Delta^7Li_{fine\text{-}source}$) can be examined as a function of the weathering regime. A significant negative relationship is observed between the weathering intensity (W/D) and $\Delta^7Li_{fine\text{-}source}$ (Fig. 3a, $r^2 = 0.75$). This correlation is stronger than that between $\delta^7Li_{fine\_sediments}$ and W/D (Fig. 3b, $r^2 = 0.48$), showing that source rock composition indeed introduces some scatter in this relationship. Sediments from rivers characterized by high W/D have the lowest $\Delta^7Li_{fine\text{-}source}$ whereas rivers having low W/D have $\Delta^7Li_{fine\text{-}source}$ close to zero. The δ^7Li_{sed} and $\Delta^7Li_{fine\text{-}source}$ also correlate well with more traditional weathering proxies such as CIA ($r^2 = 0.76$, not shown) or K/Th ratio ($r^2 = 0.62$, not shown). We observe no relationship between $\Delta^7Li_{fine\text{-}source}$ and chemical silicate weathering rates.

To explain this relationship, we suggest that at high denudation rate (and hence low W/D), incorporation of Li into secondary minerals is hindered by short mineral residence times in soils making the dissolved δ^7Li close to $\delta^7Li_{source\_material}$ (Bouchez et al., 2013; Dellinger et al., 2015; Wang et al., 2015). Therefore, the small amount of secondary minerals formed should have a low δ^7Li, which could be expected to be reflected in the δ^7Li of fine sediments (Dosseto et al., 2015). We suggest that this is not observed because at very low weathering intensity (W/D < 0.01), typical of high-erosion settings, the sediments carried by the rivers contain a high proportion of primary minerals ($\Delta^7Li_{sed\text{-}rock} = 0$) compared to secondary minerals formed during the modern weathering

Publisher: GSA
Journal: GEOL: Geology
DOI:10.1130/G38671.1

cycle, even in the fine sediments (Dellinger et al., 2014, 2015). At high weathering intensity (W/D > 0.1) such as in lowland areas, secondary minerals formed during the present-day weathering cycle and characterized by low $\delta^7Li_{fine\_sediments}$, compose the majority of the sediments and therefore control the bulk sediment Li isotope signature. The contribution of unweathered debris to river fine sediment load is likely to be more prominent for rivers draining fine-grained sedimentary rocks (which is the case of large, lithologically mixed rivers), as these lithologies are highly erodible and produce fine sediments.

IMPLICATIONS AND CONCLUSIONS

These results have important implications regarding the use of Li isotopes in clastic sediments to trace weathering regimes both in the present-day and in the past. First, the δ^7Li of modern river sediments is primarily related to weathering intensity (that is, in the modern Earth, mostly a function of the erosion rate; Dixon and von Blanckenburg, 2012) and not to the silicate weathering rate as inferred by other studies (e.g., Dosseto et al., 2015).

Second, the δ^7Li of fine river sediments is sensitive only to large changes of the weathering intensity (i.e., by an order of magnitude; Fig. 3a.). In particular, a $\Delta^7Li_{fine\text{-}source}$ value between −1‰ and −3.5‰ can correspond to a large range of possible weathering intensity comprised between 0.005 and 0.08. Indeed, in high-erosion rate settings, the contribution of soil-derived weathered particles is minor compared to that of debris of unweathered bedrock mobilized by mass wasting processes, even in the finest river sediments fraction (Dixon and von Blanckenburg, 2012; Dellinger et al., 2014). However, the δ^7Li of clastic sediments can clearly discriminate between high weathering intensity

Publisher: GSA
Journal: GEOL: Geology
DOI:10.1130/G38671.1

settings (typical of tropical lowland areas like the Congo River basin) and intermediate to low weathering intensity regimes.

The third important implication is related to the use of Li isotopes in detrital sediments as a proxy for palaeo-weathering regimes. Tracing ancient weathering processes using conventional geochemical tracers in detrital sediments (*e.g.* chemical index of alteration CIA, or chemical ratios combining a soluble and an insoluble element, such as Na/Sm, U/Th or K/Al) can be challenging because these proxies are also influenced by sediment provenance, grain size effects or post-depositional alteration (Bouchez et al., 2011a; Carpentier et al., 2013; Li and Yang, 2010; Lupker et al., 2013). Hence, some recent studies have used Li isotopes in fluvial alluvial deposits (Dosseto et al., 2015), marine detrital sediments (Bastian et al., 2015) or ancient siliciclastic rocks (Li et al., 2016) to determine palaeo-weathering conditions. In comparison to marine carbonates, clastic sediments record the fingerprint of local weathering conditions and have the advantage of not being influenced by biological fractionation ("vital effects") observed during carbonate precipitation (Vigier et al., 2015).

The results from this study can be used as a framework for interpreting the detrital $\delta^7Li_{fine\_sediments}$ and Li/Al ratio in sediment archives. It demonstrates the importance of correcting for grain size and lithological variability in order to interpret the detrital Li isotope composition in terms of weathering intensity. It also shows that the $\Delta^7Li_{fine\text{-}source}$ value is a function of the weathering intensity only for W/D values higher than 0.05. Overall, the combined use of Li/Al, δ^7Li and other more traditional weathering proxies (like CIA) has great potential for quantifying both sedimentary recycling and weathering intensity in sediment archives.

Publisher: GSA
Journal: GEOL: Geology
DOI:10.1130/G38671.1

ACKNOWLEDGMENTS

We thank Catherine Chauvel, Philip Pogge von Strandmann, Paul Tomascak, and an anonymous reviewer for constructive comments, and Éric Gayer for his help with map design. This study was funded by the CNRS-INSU program Syster. This is IPGP contribution 3815.

REFERENCES CITED

Allègre, C.J., Dupré, B., Négrel, P., and Gaillardet, J., 1996, Sr-Nd-Pb isotope systematics in Amazon and Congo River systems: Constraints about erosion processes: Chemical Geology, v. 131, p. 93–112, doi:10.1016/0009-2541(96)00028-9.

Bastian, L., Revel, M., and Vigier, N., 2015, Investigating Li isotope composition of Nile deltaic sediments as paleotracer of continental alteration: Procedia Earth and Planetary Science, 11th Applied Isotope Geochemistery Conference AIG-11, v. 13, p. 261–264. doi:10.1016/j.proeps.2015.07.061.

Berner, R.A., Lasaga, A.C., and Garrels, R.M., 1983, The carbonate-silicate geochemical cycle and its effect on atmospheric carbon dioxide over the past 100 million years: American Journal of Science, v. 283, p. 641–683, doi:10.2475/ajs.283.7.641.

Bouchez, J., von Blanckenburg, F., and Schuessler, J.A., 2013, Modeling novel stable isotope ratios in the weathering zone: American Journal of Science, v. 313, p. 267–308, doi:10.2475/04.2013.01.

Bouchez, J., Gaillardet, J., France-Lanord, C., Maurice, L., and Dutra-Maia, P., 2011a, Grain size control of river suspended sediment geochemistry: Clues from Amazon

River depth profiles: Geochemistry Geophysics Geosystems, v. 12, Q03008, doi:10.1029/2010GC003380.

Carpentier, M., Weis, D., and Chauvel, C., 2013, Large U loss during weathering of upper continental crust: The sedimentary record: Chemical Geology, v. 340, p. 91–104, doi:10.1016/j.chemgeo.2012.12.016.

Chetelat, B., Liu, C.Q., Wang, Q., and Zhang, G., 2013, Assessing the influence of lithology on weathering indices of Changjiang river sediments: Chemical Geology, v. 359, p. 108–115, doi:10.1016/j.chemgeo.2013.09.018.

Dellinger, M., Gaillardet, J., Bouchez, J., Calmels, D., Galy, V., Hilton, R.G., Louvat, P., and France-Lanord, C., 2014, Lithium isotopes in large rivers reveal the cannibalistic nature of modern continental weathering and erosion: Earth and Planetary Science Letters, v. 401, p. 359–372, doi:10.1016/j.epsl.2014.05.061.

Dellinger, M., Gaillardet, J., Bouchez, J., Calmels, D., Louvat, P., Dosseto, A., Gorge, C., Alanoca, L., and Maurice, L., 2015, Riverine Li isotope fractionation in the Amazon River basin controlled by the weathering regimes: Geochimica et Cosmochimica Acta, v. 164, p. 71–93, doi:10.1016/j.gca.2015.04.042.

Dixon, J.L., and von Blanckenburg, F., 2012, Soils as pacemakers and limiters of global silicate weathering: Comptes Rendus Geoscience, v. 344, p. 597–609, doi:10.1016/j.crte.2012.10.012.

Dosseto, A., Vigier, N., Joannes-Boyau, R., Moffat, I., Singh, T., and Srivastava, P., 2015, Rapid response of silicate weathering rates to climate change in the Himalaya: Geochemical Perspectives Letters, v. 1, p. 10–19, doi:10.7185/geochemlet.1502.

294 Gaillardet, J., Millot, R., and Dupré, B., 2003, Chemical denudation rates of the western
295 Canadian orogenic belt: The Stikine terrane: Chemical Geology, v. 201, p. 257–279,
296 doi:10.1016/j.chemgeo.2003.07.001.
297 Garçon, M., and Chauvel, C., 2014, Where is basalt in river sediments, and why does it
298 matter?: Earth and Planetary Science Letters, v. 407, p. 61–69,
299 doi:10.1016/j.epsl.2014.09.033.
300 Henchiri, S., Gaillardet, J., Dellinger, M., Bouchez, J., and Spencer, R.G.M., 2016,
301 Temporal variations of riverine dissolved lithium isotopic signatures unveil
302 contrasting weathering regimes in low-relief Central Africa: Geophysical Research
303 Letters, v. 43, p. 4391–4399, doi:10.1002/2016GL067711.
304 Holland, H. D. 1984, The chemical evolution of the atmosphere and oceans. Princeton
305 University Press.
306 Huh, Y., Chan, L.-H., and Edmond, J.M., 2001, Lithium isotopes as a probe of
307 weathering processes: Orinoco River: Earth and Planetary Science Letters, v. 194,
308 p. 189–199, doi:10.1016/S0012-821X(01)00523-4.
309 Filizola, N., 2003, Transfert sédimentaire actuel par les fleuves amazoniens [Ph.D.
310 Thesis]: Toulouse, France, Universite Toulouse III-Paul Sabatier, 273 p.
311 Li, C., and Yang, S., 2010, Is chemical index of alteration (CIA) a reliable proxy for
312 chemical weathering in global drainage basins?: American Journal of Science,
313 v. 310, p. 111–127, doi:10.2475/02.2010.03.
314 Li, G., and West, A.J., 2014, Evolution of Cenozoic seawater lithium isotopes: Coupling
315 of global denudation regime and shifting seawater sinks: Earth and Planetary Science
316 Letters, v. 401, p. 284–293, doi:10.1016/j.epsl.2014.06.011.

317 Li, S., Gaschnig, R.M., and Rudnick, R.L., 2016, Insights into chemical weathering of the
318 upper continental crust from the geochemistry of ancient glacial diamictites:
319 Geochimica et Cosmochimica Acta, v. 176, p. 96–117,
320 doi:10.1016/j.gca.2015.12.012.
321 Lupker, M., France-Lanord, C., Galy, V., Lavé, J., and Kudrass, H., 2013, Increasing
322 chemical weathering in the Himalayan system since the Last Glacial Maximum:
323 Earth and Planetary Science Letters, v. 365, p. 243–252,
324 doi:10.1016/j.epsl.2013.01.038.
325 Misra, S., and Froelich, P.N., 2012, Lithium isotope history of Cenozoic seawater:
326 Changes in silicate weathering and reverse weathering: Science, v. 335, p. 818–823,
327 doi:10.1126/science.1214697.
328 Pogge von Strandmann, P.A.E., Jenkyns, H.C., and Woodfine, R.G., 2013, Lithium
329 isotope evidence for enhanced weathering during Oceanic Anoxic Event 2: Nature
330 Geoscience, v. 6, p. 668–672, doi:10.1038/ngeo1875.
331 Pogge von Strandmann, P.A.P., and Henderson, G.M., 2015, The Li isotope response to
332 mountain uplift: Geology, v. 43, p. 67–70, doi:10.1130/G36162.1.
333 Sauzéat, L., Rudnick, R.L., Chauvel, C., Garçon, M., and Tang, M., 2015, New
334 perspectives on the Li isotopic composition of the upper continental crust and its
335 weathering signature: Earth and Planetary Science Letters, v. 428, p. 181–192,
336 doi:10.1016/j.epsl.2015.07.032.
337 Tomascak, P.B., Magna, T., and Dohmen, R., 2016, Advances in Lithium Isotope
338 Geochemistry: Cham, Switzerland, Springer International Publishing, 195 p,
339 doi:10.1007/978-3-319-01430-2.

340 Vigier, N., Rollion-Bard, C., Levenson, Y., and Erez, J., 2015, Lithium isotopes in
341 foraminifera shells as a novel proxy for the ocean dissolved inorganic carbon (DIC):
342 Comptes Rendus Geoscience, v. 347, p. 43–51, doi:10.1016/j.crte.2014.12.001.
343 Wang, Q.-L., Chetelat, B., Zhao, Z.-Q., Ding, H., Li, S.-L., Wang, B.-L., Li, J., and Liu,
344 X.-L., 2015, Behavior of lithium isotopes in the Changjiang River system: Sources
345 effects and response to weathering and erosion: Geochimica et Cosmochimica Acta,
346 v. 151, p. 117–132, doi:10.1016/j.gca.2014.12.015.
347 West, A.J., Galy, A., and Bickle, M., 2005, Tectonic and climatic controls on silicate
348 weathering: Earth and Planetary Science Letters, v. 235, p. 211–228,
349 doi:10.1016/j.epsl.2005.03.020.
350 **FIGURE CAPTIONS**
351 Figure 1. Li isotope composition as a function of Li concentration for large river
352 sediments. Gray color scale applies only to rivers draining mountain ranges (circles in
353 figure) and corresponds to the logarithm of the D_{90} values (which is the grain size below
354 which 90% of the grains are found in a given sample). For lowland rivers, grain size was
355 not measured, but all lowlands sediment are surface samples, which are generally fine-
356 grained (Filizola, 2003).
357
358 Figure 2. A: The Li/Al ratio in fine sediments as a function of the proportion of shales in
359 the source of river sediments, as calculated using Nd isotopes or trace element ratios (see
360 the Data Repository [see footnote 1]). Black dotted line corresponds to the mixing
361 between shales and igneous rocks. Gray dotted lines labeled with numbers correspond to
362 the Li weathering index values $(Li/Al)_{sediment\_load}$ / $(Li/Al)_{source\_material}$ for various

Publisher: GSA
Journal: GEOL: Geology
DOI:10.1130/G38671.1

proportion of shales. The best fit of the data ($R^2 = 0.82$), excluding the lowland rivers, corresponds to a Li weathering index value of 0.9. The average igneous rock and shale end members as given in Dellinger et al. (2014) and Sauzéat et al. (2015) are also represented. B: Li weathering index $(Li/Al)_{sediment\_load}$ / $(Li/Al)_{source\_material}$ in the sediments as a function of the weathering intensity.

Figure 3. A: Li isotope composition of fine large river sediments corrected from the source rock ($\Delta^7Li_{fine\text{-}source}$). B: Li isotope composition of large river fine sediments ($\delta^7Li_{sediment\_load}$), as a function of the weathering intensity (W/D).

[1]GSA Data Repository item 2017xxx, methods, supplementing text, Figures DR1–DR6 and Tables DR1 and DR2, is available online at http://www.geosociety.org/datarepository/2017/ or on request from editing@geosociety.org.

Figure 1

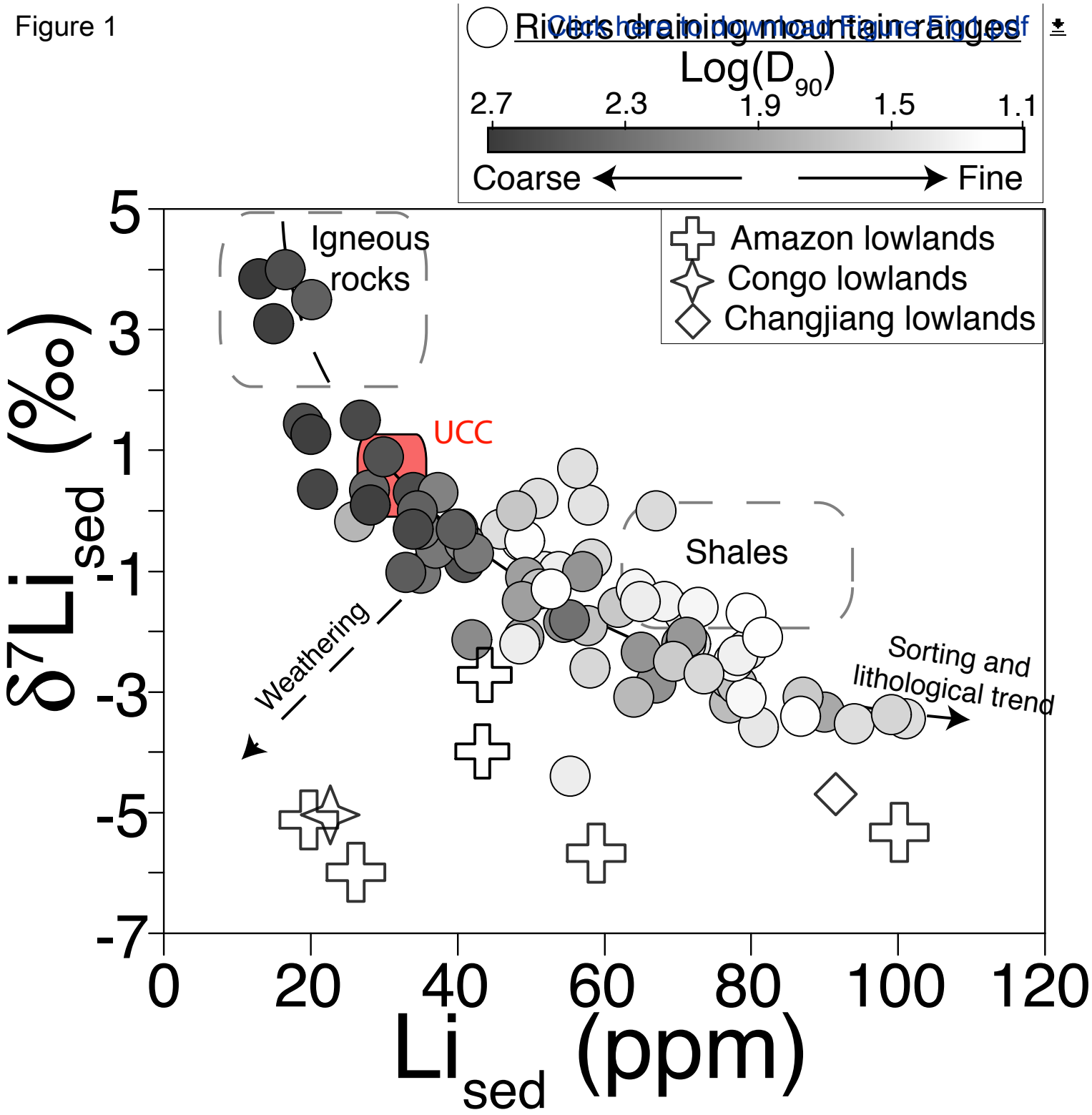
Rivers draining mountain ranges
Log(D90)
2.7
2.3
1.9
1.5
1.1
Coarse
Fine
Amazon lowlands
Congo lowlands
Changjiang lowlands
Igneous rocks
UCC
Shales
Weathering
Sorting and lithological trend
δ7Lised (‰)
Lised (ppm)
5
3
1
-1
-3
-5
-7
0
20
40
60
80
100
120

Figure 2

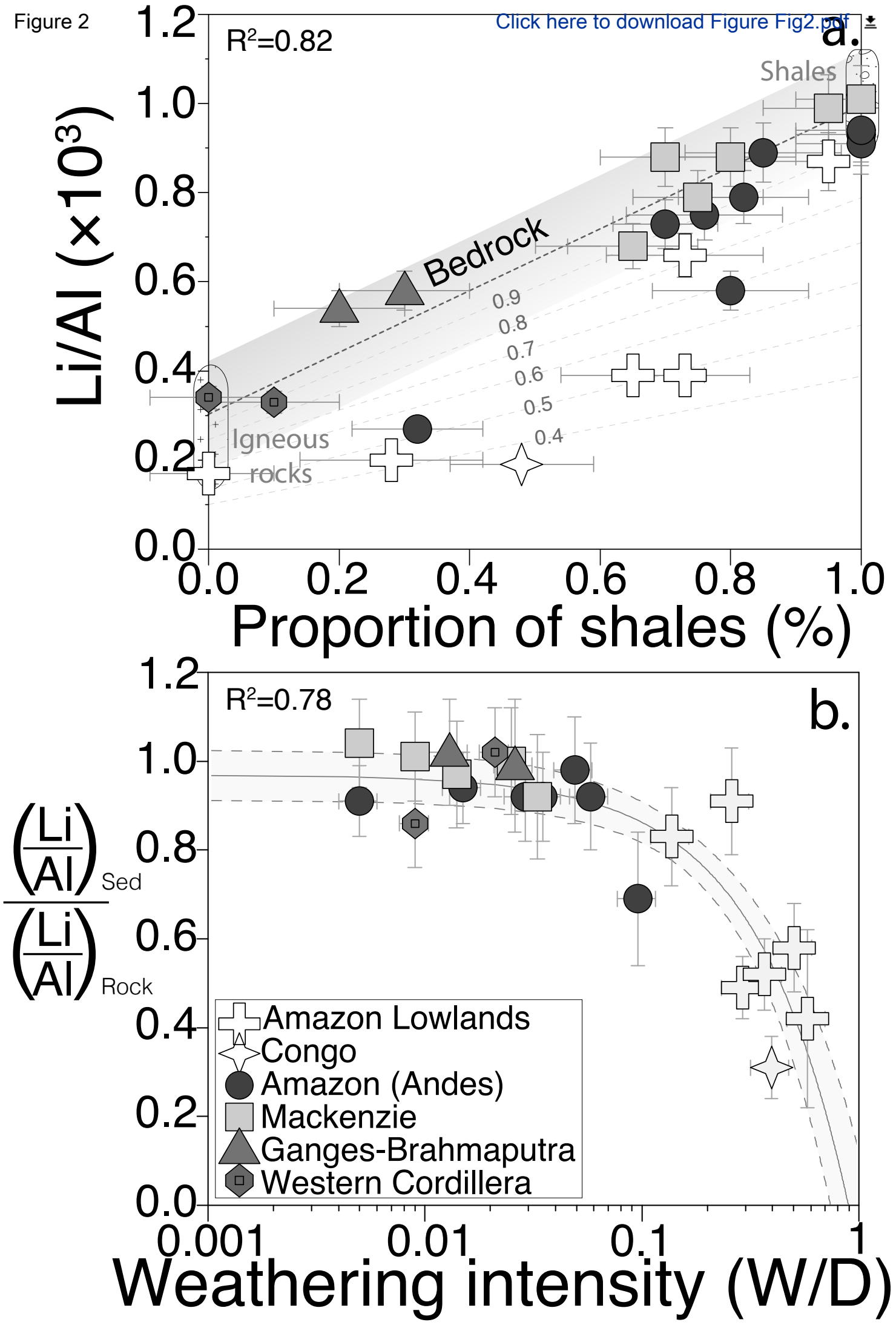

Figure 3

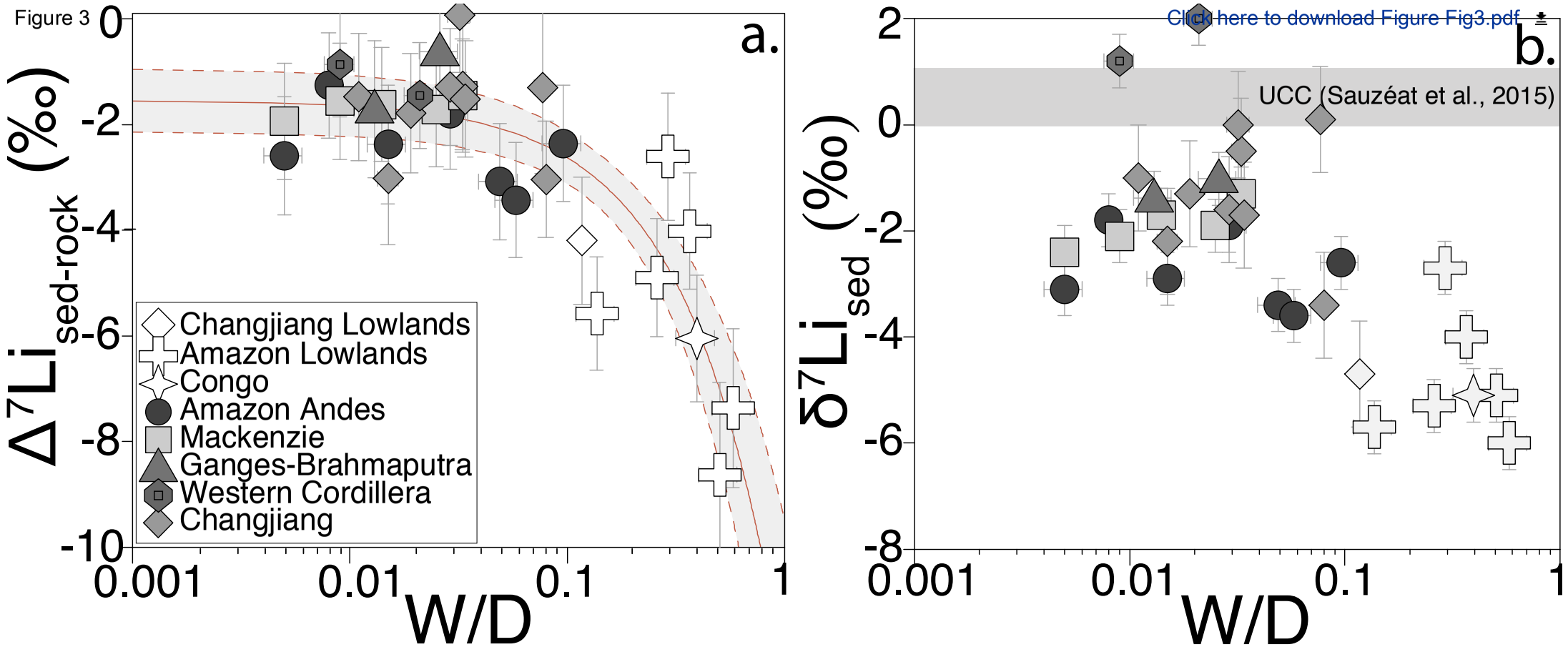
a.
b.
Click here to download Figure Fig3.pdf
UCC (Sauzéat et al., 2015)
Changjiang Lowlands
Amazon Lowlands
Congo
Amazon Andes
Mackenzie
Ganges-Brahmaputra
Western Cordillera
Changjiang
Δ7Lised-rock (‰)
δ7Lised (‰)
W/D
0
-2
-4
-6
-8
-10
2
0.001
0.01
0.1
1

Tracing weathering regimes using the Li isotope composition of detrital sediments

Mathieu Dellinger, Julien Bouchez, Jérôme Gaillardet, Laetitia Faure and Julien Moureau

GSA Data Repository

Contents

1. Analytical methods

Here, we briefly describe the analytical methods used for measurements of the Li and Nd isotope composition of sediments.

Li isotopes: the digestion, column chemistry and Li isotope measurement procedure for the sediments has been described in Dellinger et al., (2014). About 20 mg of sediment were digested in HF-HNO_3 at 100°C during 24 to 48 hours. Li was then separated from the matrix by ion-exchange chromatography using a method modified from James and Palmer (2000) and described in Dellinger et al. (2014). The lithium isotope composition was measured using a MC-ICP-MS Neptune (Thermo Scientific, Bremen) at IPGP (Paris). Details on the analytical procedure are available in Dellinger et al. (2014). Accuracy and reproducibility of the isotopic measurements were checked through repeated analyses of the basalt reference materials JB-2 yielded δ^7Li = +4.47±0.53 (± 2σ, n = 30 separations and 15 digestions).

Nd isotopes: Nd isotope composition was measured in the same aliquot used for Li isotopes. Nd was separated from the rest of the matrix by ion-exchange chromatography using the TRU-spec and Ln-spec resins and measured by MC ICP-MS Neptune in IPGP following the method described in Cogez et al., (2015).

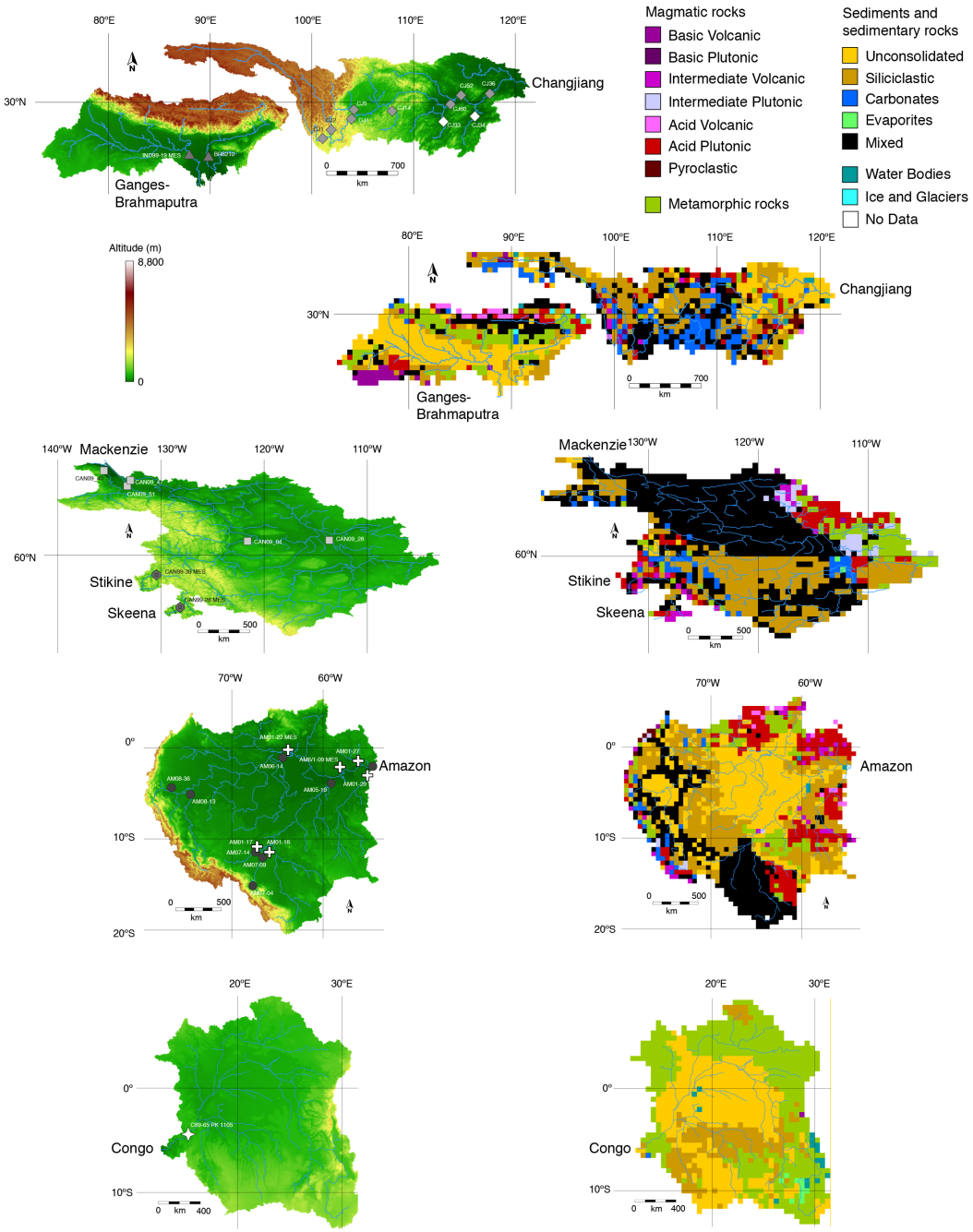

Figure DR1: Maps of the river basins (elevation on the left, geology on the right) from this study, with the locations of the samples. The Geological maps are from Hartmann and Moosdorf (2013). The Changjiang samples are from Wang et al., (2015)

2. Provenance of fine river sediments

Here, we describe how the relative proportion of river sediment derived from the erosion of shales, igneous and high-grade metamorphic rocks is calculated for each river basin. The location of the samples and the geological map of each river basin are shown in Fig. (DR1).

Amazon River: In the Amazon basin, the major rock types are sedimentary rocks in the Andes and foreland/lowlands, igneous rocks (andesites in the northern part of the Amazonian Andes and granitoids in their southern part) and granitic and metamorphic rocks in the Brazilian and Guyana shields. The Nd isotope composition (expressed here as $\varepsilon_{Nd}(0)$, the ratio in parts per 10^4 (units) between the measured $^{143}Nd/^{144}Nd$ of the sample relative to the present-day value (0.512638) of the $^{143}Nd/^{144}Nd$ of the CHondritic Uniform Reservoir (CHUR)) is a reliable tracer of the provenance of river sediments in the Amazon basin because the major rock types have distinct ε_{Nd} values (Allègre et al., 1996; Roddaz et al., 2005; Viers et al., 2008). In the following we consider that river sediments in the Amazon Basin result from a binary mixture between two end members, such that the following mixing equation can be written:

$$\varepsilon_{Nd}(0)_{sed} = \varepsilon_{Nd}(0)_{sha} \times \gamma_{sha} + \varepsilon_{Nd}(0)_{Ign} \times (1 - \gamma_{sha})$$

With $\varepsilon_{Nd}(0)_{sed}$, $\varepsilon_{Nd}(0)_{sha}$ and $\varepsilon_{Nd}(0)_{Ign}$, respectively the Nd isotope composition of river sediment, shale and igneous rock. The proportion of shales-derived particles ("γ_{sha}" in mass %) can be calculated as:

$$\gamma_{sha}^{Nd} = \gamma_{sha} \times \frac{[Nd]_{sha}}{[Nd]_{sed}}$$

As the average Nd concentration of shale and igneous rocks is not significantly different (Condie, 1993), we consider that $\gamma_{sha} = \gamma_{sha}^{Nd}$. As explained below, the composition of the igneous end member ($\varepsilon_{Nd}(0)_{Ign}$) varies between the different sub-basins, while the composition of the shale end member ($\varepsilon_{Nd}(0)_{sha}$) is considered homogenous throughout the Amazon River basin.

The Beni River drains exclusively shales from the Bolivian Andes and we use the $\varepsilon_{Nd}(0)$ of its sediments to estimate the average $\varepsilon_{Nd}(0)$ value of Andean sedimentary rocks. The $\varepsilon_{Nd}(0)$ of Beni sediments ranges between −12.2 and −12.9, in good agreement with the range of $\varepsilon_{Nd}(0)$ values measured in Andean sedimentary rocks (−10 to −13; Pinto, 2003; Viers et al., 2008) and Neogene South Amazonian foreland basin sediments from Roddaz et al., (2005). Similarly, the

Yata river that drains exclusively the lowlands Tertiary sedimentary rocks (originated from the erosion of the region of the Andes) have a $\varepsilon_{Nd}(0)$ of −11.6, in good agreement with the $\varepsilon_{Nd}(0)$ value measured in Beni river sediments. Therefore, we assume a $\varepsilon_{Nd}(0)_{sha}$ of −12.0±1.0 for the shale end member. The same value of −12.0 was also assumed for the metasedimentary end-member of the Madre de dios river basin by Basu et al., (1990). In addition, we consider that this value is also representative of the shales from the northern Andes. Indeed, the $\varepsilon_{Nd}(0)$ of Solimões sediments defines a trend with the Al concentration (grain size proxy) that tends toward a similar shale $\varepsilon_{Nd}(0)$ value (Fig. DR2) and Neogene North Amazonian foreland basin sediments from Roddaz et al., (2005) also plot on the same trend.

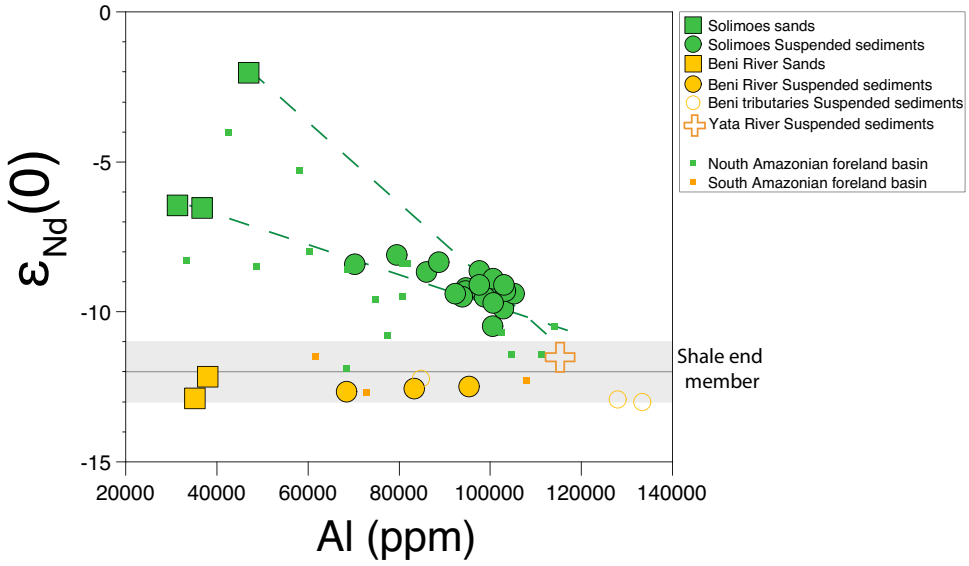

Figure DR2: $\varepsilon_{Nd}(0)$ as a function of the Al concentration in sediments. Solimões and Beni data are from Bouchez et al., (2011a), Dellinger et al., (2015) and Viers et al., (2008). Data for foreland basin sediments are from Roddaz et al., (2005). The grey band corresponds to the estimated $\varepsilon_{Nd}(0)$ of the mean shale end-member in the Amazon basin.

Regarding the igneous rock end member, the Nd isotope composition measured in Andean Neogene granitoid rocks from the Sierra Blanca in Peru have $\varepsilon_{Nd}(0)$ generally between −3 to 0 (Petford and Atherton, 1996). Pemian-Triassic and Carboniferous granitoids in southern Peru have a median $\varepsilon_{Nd}(0)$ of −4.7±0.6 (Miskovic, 2008). Accordingly, bed sediments from the

Solimões River draining the Peruvian and Ecuadorian Andes, and for which the major and trace element signature reflect an igneous rock provenance (Bouchez et al., 2011a; Dellinger et al., 2014), have $\varepsilon_{Nd}(0)$ ranging from −6.5 to −2.0. However, volcanic rocks in Ecuador (mostly andesites) have a higher $\varepsilon_{Nd}(0)$ ranging between +2 and +6 with (Bryant et al., 2006), and bed sediments from the Pastaza River derived from the erosion of andesite in Ecuador has a $\varepsilon_{Nd}(0)$ of +1.9 (Dellinger et al., 2015a). This high $\varepsilon_{Nd}(0)$ indicates that Pastaza sediments predominantly derive from the erosion of more recent (Quaternary) andesite. In the following, we use a $\varepsilon_{Nd}(0)_{Ign}$ of −3.0±2.0 for the igneous end member of all the Andean-fed rivers, except for the Pastaza River for which we use a $\varepsilon_{Nd}(0)_{Ign}$ value of +2.0±1.0.

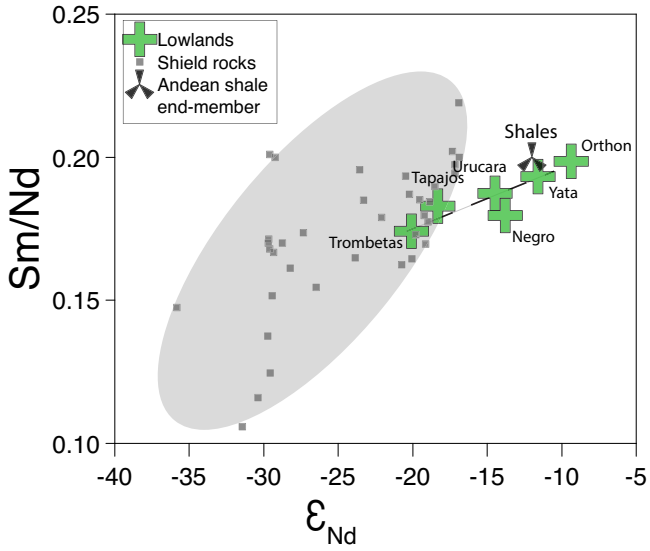

Fig. DR3: Sm/Nd as a function of the ε_{Nd} of lowland river sediments. Shield rock data are from Santos et al., (2000). The Tapajós and Pastaza rivers have a εNd(0) and Sm/Nd close to the signature of shield rocks whereas Urucara and Negro river sediments contain shale-derived sediments. The shale end-member corresponds to the average composition of Beni river sediments.

Regarding the shield regions, the range of $\varepsilon_{Nd}(0)$ measured in rock samples from the Rio Negro, Central Amazon and Tapajos-Parima provinces is very large (−20 to −30) and positively correlated to the Sm/Nd ratio as a result of magmatic differentiation (Allègre et al., 1996; Basu et al., 1990; Hoorn et al., 2009; Roddaz et al., 2005; Santos et al., 2000). The Sm/Nd ratio of rivers

draining the shield range between 0.15 to 0.20, and for a given Sm/Nd ratio, lowlands rivers generally have higher $\varepsilon_{Nd}(0)$ than cratonic rocks (Fig. DR3) and plot on a line trending towards the shale end member (defined as the mean Sm/Nd and $\varepsilon_{Nd}(0)$ of Beni River sediments). Only the Tapajós and Trombetas river sediments have a Nd isotope composition similar to that of the cratonic rocks in the Amazon basin whereas the Rio Negro and Urucara rivers have a $\varepsilon_{Nd}(0)$ intermediate between cratonic rocks and Andean-derived shales, consistently with the findings of Allègre et al., (1996). We consider therefore the Trombetas River composition as representative of the mean Nd isotope composition of the shield end member ($\varepsilon_{Nd}(0)_{Ign} = -20.0\pm2.0$).

Congo River: The lithology of the Congo Basin is mainly composed of Archean and Proterozoic TTG along the basin border, and of sedimentary rocks in the center. To our knowledge, there is no available Nd isotope data on Congo rocks in the literature. However, Allègre et al. (1996) report $\varepsilon_{Nd}(0)$ values for the major Congo tributaries. The $\varepsilon_{Nd}(0)$ range from −12.9 for the Lobaye River to −18.2 for the Likouala. We also measured the $\varepsilon_{Nd}(0)$ on a lateritic soil profile sampled 100 km downstream from Bangui (Henchiri et al., 2016) and developed on TTG rocks. The Nd isotope values range from −18.1 to −18.9 (See table DR2) and is similar to the value of the Likouala.

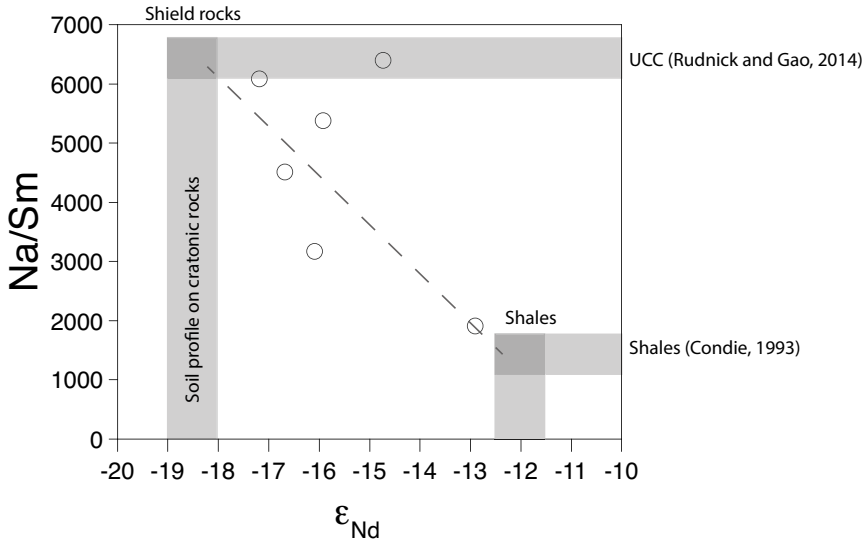

Fig. DR4: Crustal Na/Sm for Congo rivers inferred by Gaillardet et al. (1995) as a function of the sediment ε_{Nd}. The Nd isotope composition of the cratonic end member is estimated to be −18.5±0.5 based on the above trend, the Na/Sm of UCC (Rudnick and Gao, 2014) and the Nd

isotope composition of a soil profile developed on cratonic rocks in Bangui (this study). The Nd isotope composition of the shales end-member is estimated to be −12±0.5 by projecting the typical Na/Sm value of global Phanerozoic shales (from Condie, 1993) on the mixing trend. This value is also compatible with the Nd isotope composition of the Lobaye River.

Interestingly, the $\varepsilon_{Nd}(0)$ of Congo tributaries sediments is negatively correlated to the Na/Sm ratio of the Congo tributaries continental crust (sediments + dissolved) inferred by Gaillardet et al., (1995) (Fig. DR4). This crustal Na/Sm ratio can be used to distinguish TTG (high Na/Sm) from shales (low Na/Sm resulting from Na depletion during ancient weathering processes). The Likouala has a TTG-like Na/Sm signature whereas the Lobaye has a signature close to that of shales. Altogether, the range of variation of $\varepsilon_{Nd}(0)$ in Congo sediments can be explained at first order as resulting from a mixture between a TTG igneous end member of high $\varepsilon_{Nd}(0)_{Ign}$ around −19 and a metasedimentary end member of low $\varepsilon_{Nd}(0)_{sha}$ (around −12), as for the Amazon. Using eqs. (1) and (2), we calculate that the proportion of shale-derived particles in the Congo River sediments is 40±10%. We note that the correlation between $\varepsilon_{Nd}(0)$ and Na/Sm is scattered and therefore that this method for determining the provenance of Congo River sediments gives only a first-order estimate of the proportion of shale-derived particles.

Ganges-Brahmaputra rivers: In the Ganges-Brahmaputra system, the source of sediments has been characterized using Nd and Sr isotopes by previous studies (Galy and France-Lanord, 2001; Lupker et al., 2013; Singh et al., 2008; Singh and France-Lanord, 2002). The Ganges sediments are mostly derived from the erosion of the high-grade metamorphic rocks from the High Himalaya Crystalline (HHC, about 70%) and the rest of the sediments from the low-grade metasedimentary rocks of the Lesser Himalayas (LH, 30%). For the Brahmaputra, Singh and France-Lanord (2002) estimate that in average, between 50 and 70% of the sediments are derived from the erosion of the HHC, about 10% from the LH and the rest from the erosion of the Trans-Himalayan Batholith (igneous rocks). However, the provenance of the Brahmaputra sediments can be quite variable depending upon the depth and the sampling date (Lupker et al., 2013). As the Nd and Sr isotope composition of the Brahmaputra sediment sample from this study (BR8210) has been measured by Lupker et al., (2013), we can use these data along with the estimate of the Himalayan rock end-members (Galy and France-Lanord, 2001; Singh et al., 2008; Singh and France-Lanord, 2002) to determine the provenance for this sample. We calculate that

for this Brahmaputra sample, the proportion of LH, and therefore of shales-derived sediments, is 20±10%.

Mackenzie River: The upper crust drained by the main Mackenzie tributaries is composed by a mixture between shales and igneous rocks having granodioritic to granitic composition (Driver et al., 2000; Reeder et al., 1972). The Nd and Sr isotope composition has not been measured on sediments from the Mackenzie tributaries. However, a large dataset of shale chemical composition from the Liard River basin is available in Ross and Bustin, (2009). Dellinger, (2013) shows that some insoluble elements (Cr, Ti, Eu, Cs) have significantly distinct concentration between shales and granitic rocks. It is therefore possible to use these element contents to calculate the proportion of shale-derived and igneous rock-derived particles in the fine sediments of the Mackenzie rivers (Fig. DR.5). The Peel River that drain almost exclusively shales have sediments having chemical signature similar to the mean composition of shales from Ross and Bustin (2009). Other rivers have lower Al-normalized concentrations showing that they contain a larger, yet small fraction of igneous-derived material compared to the Peel. We estimate the composition of the shale end member using the data from Ross and Bustin (2009), Garzione et al., (1997) and Morrow, (1999). For the shale end member, we estimate that Ti/Al = 0.057±0.002 (median value ± 2σ/√n, n=101), Cr/Al = 1.54±0.12×10^{-3} (n=106) and Cs/Al = 0.10±0.01×10^{-3} (n=50). For the granitic end member, we use data from Driver et al., (2000) and Heffernan, (2004): Ti/Al = 0.030±0.005 (n=60), Cr/Al = 0.13±0.29×10^{-3} (n=23) and median Cs/Al = 0.050±0.005×10^{-3} (n=50). We calculate that the Mackenzie tributaries contain between 70 and 100% of shale-derived sediments.

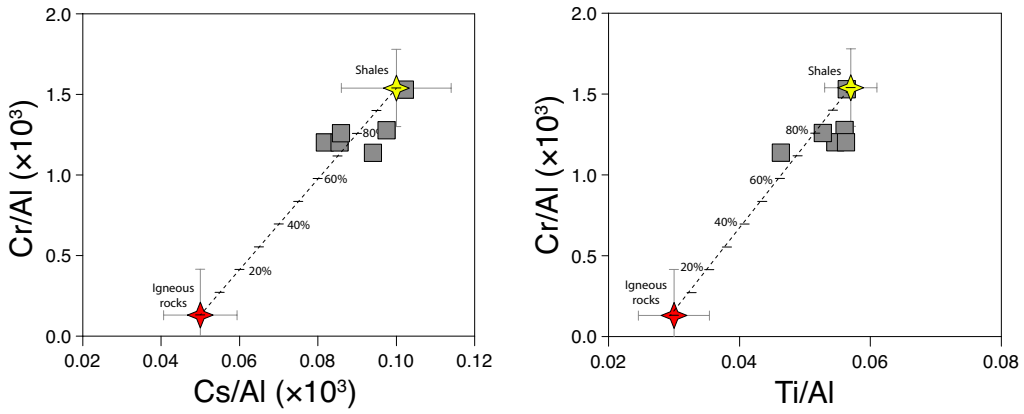

Fig. DR5: Cr/Al as a function of the Cs/Al and Ti/Al ratio for Mackenzie River fine sediments. The igneous and shales end members are also represented (as discussed in the section 2 of the data repository).

Western Cordillera: Most of the bedrock of the Canadian western cordillera rivers is formed of volcanic rocks, with a minor contribution of shales. The Sr isotope composition of both dissolved and suspended material for the Skeena and Stikine rivers is unradiogenic (<0.707; Gaillardet et al., 2003) so we consider that the proportion of shales is lower than 10±10%.

Changjiang: For the Changjiang, we determined the proportion of shales by using the Li concentration in sediments and the relation between the Li concentration and proportion of shales defined by other rivers (see section "The influence of lithology" in the main text). We note that samples CJ33 and CJ34 correspond to rivers draining lowland areas (Wang et al., 2015). Hence, the provenance method based on Li might not be applicable to these rivers. However, their weathering intensity is quite low compared to lowland rivers of the Amazon. In addition, the Li content of the sediments is higher than 85 ppm indicating that even if they have lost a significant proportion of Li, their main source is the erosion of shales (in agreement with the lithology in these two river basin; Wang et al., 2015). Based on the uncertainty on the trend between Li concentration and proportion of shales defined by other rivers, the estimated uncertainty on the proportion of shale-derived particles for Changjiang samples is ±15%.

3. Calculation of the δ^7Li_{rock} and $(Li/Al)_{rock}$

To calculate the Li isotope composition of the bedrock, δ^7Li_{rock} (which is the δ^7Li that the sediments would have in absence of chemical weathering) and $(Li/Al)_{rock}$ values, we can use the proportion of shales calculated before (γ_{sha}) in combination with the mixing equation in Dellinger et al., (2014):

$$\left(\frac{Li}{Al}\right)_{rock} = \left(\frac{Li}{Al}\right)_{sha} \times \gamma_{sha} + \left(\frac{Li}{Al}\right)_{Ign} \times (1 - \gamma_{sha})$$

and

$$(\delta^7Li)_{rock} = (\delta^7Li)_{sha} \times \left(\frac{(Li/Al)_{sha}}{(Li/Al)_{sed}}\right) \times \gamma_{sha} + (\delta^7Li)_{Ign} \times \left(\frac{(Li/Al)_{Ign}}{(Li/Al)_{sed}}\right) \times (1 - \gamma_{sha})$$

With the shale end member composition being δ^7Li of −0.5±1‰ and Li/Al of 1.0±0.1×10^{-3} and the igneous end member δ^7Li of +3.5±1.5‰, Li/Al of 0.30±0.12×10^{-3} (Dellinger et al., 2014; Sauzéat et al., 2015). For the Congo River, Henchiri et al., (2016) show that the TTG of the Congo basin have possibly high δ^7Li (+6 to +7‰) due to their Archean age. Therefore, we use a higher δ^7Li_{ign} end member of +5±2‰ for the Congo River.

For the Ganges-Brahmaputra (G-B) system, we note that G-B sands, which are derived mostly from the erosion of high-grade metasedimentary rocks, have a distinct composition (δ^7Li of 0 ± 1‰, Li/Al of 0.40 ± 0.10 × 10^{-3}; Dellinger et al., 2014) relative to igneous and sedimentary rocks. Hence, for the Ganges-Brahmaputra, we consider a mixing between a shale end member and a high-grade metamorphic end member having a δ^7Li of 0±1‰ and a Li/Al ratio of 0.40±0.10×10^{-3} (Dellinger et al., 2014).

4. Comparison between the Li depletion in sediments and the fraction of Li transported into the dissolved load

As Li is a soluble element, Li concentration in river sediments is sensitive to weathering. In particular, for a given proportion of shales, lowland rivers have a lower Li/Al ratio than rivers draining mountain ranges (Fig. 2). Yet, this Li-depletion in lowland rivers could be explained by i) the loss of Li by weathering processes and/or ii) an incorrect estimation of the bedrock (*i.e.* the proportion of shales and/or the composition of the rock end members). Following the approach of Gaillardet et al., (1999), we can test these two hypotheses using a steady state assumption. At steady state, the fraction of Li transported as dissolved should be equal to the Li depletion (Li weathering index $(Li/Al)_{sed}/(Li/Al)_{rock}$, see main text) in the sediments. The proportion of Li riverine export occurring as dissolved (w^{Li} as defined by Bouchez et al., 2013) can be calculated using the Li concentration in the dissolved and suspended load and the concentration of suspended sediment transported by the rivers.

$$w^{\mathrm{Li}} = \frac{1}{1 + \frac{[\mathrm{Li}]_{\mathrm{sed}}}{[\mathrm{Li}]_{\mathrm{diss}}} \times [\mathrm{SPM}]}$$

With $[Li]_{sed}$, $[Li]_{diss}$ and [SPM] being respectively the Li concentrations in sediment, and dissolved load, and the suspended sediment concentration. The comparison between ($1\text{-}w^{Li}$) and the weathering index (Fig. DR6) shows that at first order, there is a relatively good agreement between the amount of Li depletion in the sediments and the fraction of dissolved Li export, within uncertainties.

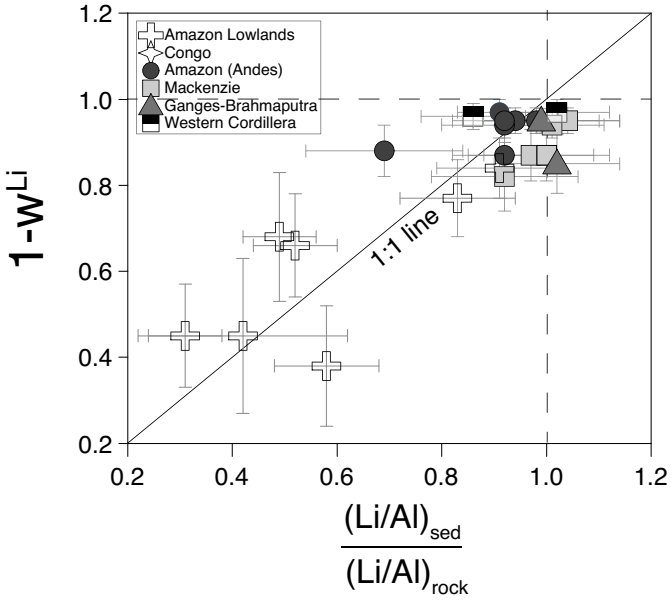

Figure DR6: Proportion of solid Li transported by the river ($1\text{-}w^{Li}$) as a function of the Li weathering index calculated as $(Li/Al)_{sed}$ / $(Li/Al)_{rock}$. The 1:1 line corresponds to the line for which ($1\text{-}w^{Li}$) is equal to $(Li/Al)_{sed}$ / $(Li/Al)_{rock}$, meaning that the fraction of Li dissolved export is compatible with that of the solid export, a requisite for steady state denudation.

This calculation does not take into account the change in Li concentration in the sediments with depth. Indeed, in large rivers draining mountain ranges, the grain size distribution of the suspended sediment load is generally bimodal with a fine mode composed of clay and silt particles and a coarse mode composed of sands (Bouchez et al., 2011a; Dellinger, 2013; Lupker et al., 2012). The fine sediments (< 63 µm) are relatively homogeneously distributed in the water

column while coarse sediments (size > 63 μm) concentration strongly increases from the surface toward the bottom of the river channel (Bouchez et al., 2011b; Galy et al., 2007; Lupker et al., 2011). As coarse sediments are mostly composed of quartz, the Li concentration in sediments decreases toward the bottom of the channel because of dilution by increasing quartz amount. This implies that the $(1\text{-}w^{Li})$ values calculated from surface sediments are underestimated. However, as shown by Dellinger et al., (2015), the difference is relatively small (less than 0.05 units of w^{Li} values). In addition, we note that in lowland rivers suspended sediments collected at any depth contain a negligible amount of coarse (> 63μm) particles (Meade, 1985). Therefore, the conclusions about the agreement between $(1\text{-}w^{Li})$ values and $(Li/Al)_{sed}$ / $(Li/Al)_{rock}$ stands whether these values are depth-integrated or calculated with surface sediments only.

Sample name	Basin	River	Location	Longitude	Latitude	References for Li isotope data	Surface	Discharge	D_{90}	Al	Li	$^{143}Nd/^{144}Nd$	$\varepsilon_{Nd}(0)$	δ^7Li	Li/Al ($\times10^{-3}$)	CIA	$[Li]_{diss}$	TDS_{Sil}
							(km^2)	(m^3/s)	(μm)	($\mu g/g$)	($\mu g/g$)			(‰)	(g/g)		(mmol/L)	(mg/L)
Amazon Lowlands																		
AM01-17	Amazon	Orthon	Riberalta	66°02'11,0" W	10°48'39,9" S	Dellinger et al., (2014, 2015)	33485	475		89835	59	0.512158	-9.37	-5.7	0.66	82	0.31	19.6
AM01-18	Amazon	Yata	Mouth	65°35'00,2" W	10°58'44,8" S	Dellinger et al., (2014, 2015)	20770	222		115390	100	0.512043	-11.61	-5.3	0.87	86	0.08	10.4
AM01-27	Amazon	Trombetas	Mouth	N.D.	N.D.	Dellinger et al., (2014, 2015)	250000	6200		115312	20	0.511609	-20.08	-5.1	0.17	92	0.037	7.8
AM01-22 MES	Amazon	Negro	Paricatuba	N.D.	N.D.	Dellinger et al., (2014, 2015)	691000	29000		113016	44	0.511930	-13.81	-2.7	0.39	87	0.031	4.3
AM6/1-09 MES	Amazon	Urucara	Mouth	N.D.	N.D.	Dellinger et al., (2014, 2015)	150000	3000		110691	43	0.511895	-14.50	-4.0	0.39	87	0.049	8.7
AM01-29	Amazon	Tapajos	Mouth	N.D.	N.D.	Dellinger et al., (2014, 2015)	490000	13500		129350	27	0.511698	-18.33	-6.0	0.20	93	0.038	11.5
Congo																		
C89-63 PK 1105	Congo	Congo	Mouth	N.D.	N.D.	Henchiri et al., (2016), this study	3700000	38026			29	0.511796	-16.43	-6.2			0.10	15.0
C89-65 PK 1105	Congo	Congo	Mouth	N.D.	N.D.	Henchiri et al., (2016), this study	3700000	38026		117769	23	0.511833	-15.70	-5.1	0.19	92	0.10	15.0
Amazon Andes																		
AM01_08	Amazon	Alto Beni	Mouth	67°40'18' W	15°07'24" S	Dellinger et al., (2014, 2015)	21197	750		84800	79	0.512011	-12.24	-1.8	0.93	74	1.62	26.4
AM07_04	Amazon	Beni	Rurrenabaque	67°32'05,2" W	14°28'26,8" S	Dellinger et al., (2014, 2015)	69980	2153	44	95289	87	0.511998	-12.49	-3.1	0.91	76	1.28	17.4
AM07_09	Amazon	Beni	Riberalta	66°05'53,8" W	10°58'44,8" S	Dellinger et al., (2014, 2015)	114379	3772	50	83319	78	0.511994	-12.56	-2.9	0.94	76	0.57	14.9
AM05_19	Amazon	Madeira	Foz Madeira	58°48′30,1" W	03°27′00,9" S	Dellinger et al., (2014, 2015)	1325000	31250	36	111822	99	0.512097	-10.55	-3.4	0.89	78	0.18	12.8
AM06_65	Amazon	Amazonas	Obidos	55°30′18,6" W	01°56′05,3" S	Dellinger et al., (2014, 2015)	4618750	182200	27	107370	81	0.512141	-9.70	-3.6	0.75	78	0.14	11.4
AM08_13	Amazon	Ucayali	Jenaro Herrera	73°40′28" W	04°54′28" S	Dellinger et al., (2014, 2015)	352593	12090	50	85664	58	0.512158	-9.37	-1.9	0.73	68	0.66	15.6
AM06_14	Amazon	Solimoes	Manacapuru	60°33′11,0" W	03°19′41,0" S	Dellinger et al., (2014, 2015)	2148000	103000	35	100535	58	0.512101	-10.48	-2.6	0.58	76	0.14	13.1
AM08_36	Amazon	Pastaza	Embouchure	N.D.	N.D.	Dellinger et al., (2014, 2015)	39000	2770	61	97031	26	0.512512	-2.45	-0.2	0.27	68	0.14	24.2
AM07_14	Amazon	Madre de Dios	Riberalta	66°05′54" W	10°57′46" S	Dellinger et al., (2014, 2015)	124231	5602	35	94447	75	0.512106	-10.38		0.79	77	0.22	14.6
Mackenzie																		
CAN09_51	Mackenzie	Red Arctic	Tsiigehtchic	133°46′44.3" W	67°25′34.2" N	Dellinger et al., (2014)	18600	159	23	79022	78.1	0.512066	-11.16	-2.4	0.99	77	0.89	8.0
CAN09_04	Mackenzie	Liard	Fort_Simpson	121°17′6.2" W	61°50′8.6" N	Dellinger et al., (2014)	275000	2450	49	64955	51.2	0.511904	-14.31	-1.7	0.79	73	0.63	8.7
CAN09_47	Mackenzie	Mackenzie	Tsiigehtchic	133°43′23.8" W	67°27′30.1" N	Dellinger et al., (2014)	1680000	8990		76477	67.5	0.512013	-12.19	-1.9	0.88	76	0.57	9.5
CAN10_32	Mackenzie	Middle Channel	Inuvik	134°4′49.8" W	68°24′33.3" N	Dellinger et al., (2014)	1805200		14	90608	79.3	0.511979	-12.86	-1.7	0.88	79		
CAN09_40	Mackenzie	Peel	Fort_McPherson	134°52′8.6" W	68°19′56.6" N	Dellinger et al., (2014)	70600	686	18	80981	81.5	0.512062	-11.23	-2.1	1.01	77	0.71	8.8
CAN09_28	Mackenzie	Slave	Fort_Smith	111°53′25.7" W	60°0′59.5" N	Dellinger et al., (2014)	616400	3200	17	77069	52.8	0.512014	-12.18	-1.3	0.68	76	0.60	12.0
Changjiang																		
CJ1	Changjiang	Jinshajiang	Panzhihua	101°37.551' E	26°34.503' N	Wang et al., (2015)	285556	1309	24	80546	48.5			-2.2	0.60	69	2.07	18.6
CJ4	Changjiang	Jinshajiang	Yibin	104°33.385' E	28°42.164' N	Wang et al., (2015)	485000	8239	22	82252	48.7			-0.5	0.59	73	0.97	18.5
CJ14	Changjiang	Changjiang	Chongqing	N.D.	N.D.	Wang et al., (2015)	867000	10945	24	84970	53.8			-1.0	0.63	71	0.78	13.4
CJ60	Changjiang	Changjiang	Yueyang	113°18.739' E	29°38.079' N	Wang et al., (2015)	1250000	15844			76.6			-1.3			0.37	14.2
CJ52	Changjiang	Changjiang	Wuhan	114°29.876' E	30°40.747' N	Wang et al., (2015)	1488000	22340	45	83606	61.9			-1.6	0.74	72	0.44	16.9
CJ36	Changjiang	Changjiang	Datong	117°38.324' E	30°46.085' N	Wang et al., (2015)	1705000	28266	26	98071	70.9			-1.7	0.72	76	0.27	16.7
CJ2	Changjiang	Yalongjiang	Panzhihua	101°49.200' E	26°40.127' N	Wang et al., (2015)	128444	1857		161917	41.3			0.1	0.26	63	0.68	17.0
CJ5	Changjiang	Minjiang	Yibin	104°33.721' E	28°48.779' N	Wang et al., (2015)	133000	2732	33	83956	67.0			0.0	0.80	67	0.45	18.3
CJ33	Changjiang	Xiangjiang	Changsha	112°56.795' E	28°07.364' N	Wang et al., (2015)	94700	2405	15	108398	86.7			-3.4	0.80	82	0.16	13.3
CJ34	Changjiang	Ganjiang	Nanchang	115°52.053' E	28°40.206' N	Wang et al., (2015)	80900	2104		103092	88.6			-4.7	0.86	80	0.25	22.4
Ganges-Brahmaputra																		
IND99-19 MES	Ganges	Ganga	Harding bridge	89°1'28.739" E	24°3'10.44" N	Dellinger et al., (2014)	1050000	15622		94322	55.0	0.511725	-17.81	-1.02	0.58		0.49	29.8
BR8210	Brahmaputra	Brahmaputra	Jamuna bg.	N.D.	N.D.	Dellinger et al., (2014)	580000	16161		87063	47	0.511897	-14.45	-1.38	0.54	66	1.08	11.8
Western cordillera																		
CAN99-28 MES	Skeena	Skeena	Kitwanga	N.D.	N.D.	This study	42200	962		83647	28.7			2.0	0.34	64	0.05	7.9
CAN99-39 MES	Stikine	Stikine	Iskut	N.D.	N.D.	This study	29300	755		75071	24.5			1.2	0.33	63	0.10	7.2

Table DR1: Data for all the clastic river sediment samples from this study. The "references" column indicate the source of Li isotope and concentration data used for this study. CIA values have been calculated using similar formula as in McLennan, (1993). Silicate weathering rates (calculated as Q× ($[Na]_{sil}$+$[K]_{sil}$+$[Ca]_{sil}$+$[Mg]_{sil}$), with "$[X]_{sil}$" the silicate-derived dissolved concentration of the element X and "Q" the discharge) and erosion rates are from multiple sources (Armijos et al., 2013; Dellinger et al., 2015b; Gaillardet et al., 1997; Guyot et al., 1996; Moquet et al., 2011; Wittmann et al., 2010). $[Li]_{diss}$ corresponds to the dissolved Li concentration, TDS_{sil} to the total dissolved load deriving from silicates weathering (in mg/L). Sediment concentration corresponds to the mean measured suspended sediment concentration for each river (in mg/L).

Sample name	River	Weathering Intensity (W/D)	Proportion of shales	δ^7Li_{rock} (‰)	$\Delta^7Li_{sed-rock}$ (‰)	$1-w^{Li}$	$(Li/Al)_{sed} / (Li/Al)_{rock}$	References
Amazon Lowlands								
AM01-17	Orthon	0.137	0.73 ± 0.12	-0.10 ± 0.89	-5.58 ± 1.07	0.77 ± 0.09	0.83 ± 0.11	Dellinger et al., (2014, 2015)
AM01-18	Yata	0.259	0.95 ± 0.14	-0.36 ± 0.93	-4.90 ± 1.12	0.84 ± 0.07	0.91 ± 0.12	Dellinger et al., (2014, 2015)
AM01-27	Trombetas	0.504	0.00 ± 0.10	3.50 ± 1.50	-8.63 ± 1.75	0.38 ± 0.14	0.58 ± 0.10	Dellinger et al., (2014, 2015)
AM01-22 MES	Negro	0.291	0.73 ± 0.10	-0.11 ± 0.90	-2.61 ± 1.20	0.68 ± 0.15	0.49 ± 0.07	Dellinger et al., (2014, 2015)
AM6/1-09 MES	Urucara	0.367	0.65 ± 0.11	0.04 ± 0.90	-4.02 ± 1.10	0.66 ± 0.12	0.52 ± 0.08	Dellinger et al., (2014, 2015)
AM01-29	Tapajos	0.581	0.28 ± 0.14	1.37 ± 1.11	-7.37 ± 1.50	0.45 ± 0.18	0.42 ± 0.20	Dellinger et al., (2014, 2015)
Congo								
C89-63 PK 1105	Congo	0.396	0.35 ± 0.10			0.51 ± 0.13		Henchiri et al., (2016), this study
C89-65 PK 1105	Congo	0.396	0.48 ± 0.11	1.00 ± 1.11	-6.05 ± 1.20	0.45 ± 0.12	0.31 ± 0.07	Henchiri et al., (2016), this study
Amazon Andes								
AM07_04	Beni	0.005	1.00 ± 0.10	-0.50 ± 1.00	-2.59 ± 1.12	0.97 ± 0.03	0.91 ± 0.08	Dellinger et al., (2014, 2015)
AM07_09	Beni	0.015	1.00 ± 0.10	-0.50 ± 1.00	-2.38 ± 1.12	0.95 ± 0.03	0.94 ± 0.08	Dellinger et al., (2014, 2015)
AM05_19	Madeira	0.049	0.85 ± 0.12	-0.30 ± 1.00	-3.08 ± 1.10	0.95 ± 0.03	0.98 ± 0.12	Dellinger et al., (2014, 2015)
AM06_65	Amazonas	0.058	0.76 ± 0.12	-0.2 ± 1.00	-3.43 ± 1.09	0.94 ± 0.03	0.92 ± 0.12	Dellinger et al., (2014, 2015)
AM08_13	Ucayali	0.029	0.70 ± 0.08	-0.10 ± 0.89	-1.80 ± 1.05	0.87 ± 0.06	0.92 ± 0.10	Dellinger et al., (2014, 2015)
AM06_14	Solimoes	0.096	0.80 ± 0.12	-0.24 ± 0.96	-2.36 ± 1.10	0.88 ± 0.06	0.69 ± 0.15	Dellinger et al., (2014, 2015)
AM08_36	Pastaza		0.32 ± 0.10	1.10 ± 0.93	-1.28 ± 1.14			Dellinger et al., (2014, 2015)
AM07_14	Madre de Dios	0.035	0.82 ± 0.10			0.95 ± 0.03	0.92 ± 0.10	Dellinger et al., (2014, 2015)
Mackenzie								
CAN09_51	Red Arctic	0.003	0.95 ± 0.10	-0.47 ± 0.91	-1.94 ± 1.10	0.95 ± 0.03	1.04 ± 0.10	Dellinger et al., (2014)
CAN09_04	Liard	0.007	0.75 ± 0.10	-0.04 ± 0.91	-1.62 ± 1.08	0.87 ± 0.06	0.97 ± 0.12	Dellinger et al., (2014)
CAN09_47	Mackenzie	0.016	0.80 ± 0.10	-0.20 ± 0.91	-1.72 ± 1.08	0.87 ± 0.06	1.00 ± 0.12	Dellinger et al., (2014)
CAN10_32	Middle Channel		0.70 ± 0.10	-0.04 ± 0.91	-1.65 ± 1.05		1.10 ± 0.12	Dellinger et al., (2014)
CAN09_40	Peel	0.006	1.00 ± 0.10	-0.50 ± 0.91	-1.56 ± 1.10	0.94 ± 0.03	1.01 ± 0.10	Dellinger et al., (2014)
CAN09_28	Slave	0.020	0.65 ± 0.10	0.15 ± 0.91	-1.45 ± 1.07	0.82 ± 0.08	0.92 ± 0.14	Dellinger et al., (2014)
Changjiang								
CJ1	Jinshajiang	0.008	0.50 ± 0.15	0.82 ± 1.13	-3.02 ± 1.26	0.80 ± 0.09		Wang et al., (2015)
CJ4	Jinshajiang	0.016	0.50 ± 0.15	0.78 ± 1.16	-1.28 ± 1.20	0.79 ± 0.09		Wang et al., (2015)
CJ14	Changjiang	0.003	0.58 ± 0.15	0.48 ± 1.03	-1.48 ± 1.20	0.92 ± 0.04		Wang et al., (2015)
CJ60	Changjiang	0.006	0.84 ± 0.15	0.49 ± 1.02	-1.79 ± 1.13	0.96 ± 0.03		Wang et al., (2015)
CJ52	Changjiang	0.012	0.68 ± 0.15	-0.3 ± 0.99	-1.29 ± 1.11	0.92 ± 0.04		Wang et al., (2015)
CJ36	Changjiang	0.010	0.78 ± 0.15	-0.2 ± 0.99	-1.52 ± 1.10	0.95 ± 0.03		Wang et al., (2015)
CJ2	Yalongjiang	0.032	0.38 ± 0.15	1.40 ± 1.20	-1.30 ± 1.63	0.64 ± 0.12		Wang et al., (2015)
CJ5	Minjiang	0.019	0.74 ± 0.15	-0.1 ± 0.97	0.07 ± 1.09	0.92 ± 0.04		Wang et al., (2015)
CJ33	Xiangjiang	0.014	0.92 ± 0.15	-0.4 ± 0.93	-3.04 ± 1.10	0.92 ± 0.04		Wang et al., (2015)
CJ34	Ganjiang	0.023	1.00 ± 0.15	-0.50 ± 1.00	-4.20 ± 1.20	0.90 ± 0.06		Wang et al., (2015)
Ganges-Brahmaputra								
IND99-19 MES	Ganga	0.026	0.30 ± 0.10	-0.40 ± 0.95	-0.62 ± 1.00	0.95 ± 0.03	0.99 ± 0.15	Dellinger et al., (2014)
BR8210	Brahmaputra	0.013	0.20 ± 0.10	0.33 ± 1.10	-1.71 ± 1.30	0.85 ± 0.07	1.02 ± 0.12	Dellinger et al., (2014)
Western cordillera								
CAN99-28 MES	Skeena	0.016	0.00 ± 0.10	3.50 ± 1.10	-1.45 ± 1.00	0.97 ± 0.03	1.02 ± 0.10	This study
CAN99-39 MES	Stikine	0.007	0.10 ± 0.10	2.06 ± 1.20	-0.86 ± 1.00	0.96 ± 0.03	0.86 ± 0.10	This study

Table DR1 (next): The parameter "$1-w^{Li}$" corresponds to the proportion of Li transported in the solid form by the river. The parameter "$(Li/Al)_{sed} / (Li/Al)_{rock}$" is the ratio between the Li/Al of the sediments and the Li/Al of the rock.

Sample name	ε_{Nd}	$^{143}Nd/^{144}Nd$
Betou 1A	-18.30	0.511700
Betou 1B	-18.13	0.511709
Betou 1C	-18.16	0.511707
Betou 2A	-18.44	0.511693
Betou 2B	-18.92	0.511668

Table DR2: Nd isotope composition of the Soil profile samples from the Congo river basin. The $\varepsilon_{Nd}(0)$ are calculated by normalizing to the CHUR value (0.512638). For details about the samples, see Henchiri et al., (2016).

References:

Allègre, C.J., Dupré, B., Négrel, P., Gaillardet, J., 1996. Sr-Nd-Pb isotope systematics in Amazon and Congo River systems: constraints about erosion processes. Chemical Geology 131, 93–112. doi:10.1016/0009-2541(96)00028-9

Armijos, E., Crave, A., Vauchel, P., Fraizy, P., Santini, W., Moquet, J.-S., Arevalo, N., Carranza, J., Guyot, J.-L., 2013. Suspended sediment dynamics in the Amazon River of Peru. Journal of South American Earth Sciences, Hydrology, Geochemistry and Dynamic of South American Great River Systems 44, 75–84. doi:10.1016/j.jsames.2012.09.002

Basu, A.R., Sharma, M., DeCelles, P.G., 1990. Nd, Sr-isotopic provenance and trace element geochemistry of Amazonian foreland basin fluvial sands, Bolivia and Peru: implications for ensialic Andean orogeny. Earth and Planetary Science Letters 100, 1–17. doi:10.1016/0012-821X(90)90172-T

Bouchez, J., Gaillardet, J., France-Lanord, C., Maurice, L., Dutra-Maia, P., 2011a. Grain size control of river suspended sediment geochemistry: Clues from Amazon River depth profiles. Geochem. Geophys. Geosyst. 12, Q03008. doi:10.1029/2010GC003380

Bouchez, J., Lupker, M., Gaillardet, J., France-Lanord, C., Maurice, L., 2011b. How important is it to integrate riverine suspended sediment chemical composition with depth? Clues from Amazon River depth-profiles. Geochimica et Cosmochimica Acta 75, 6955–6970. doi:10.1016/j.gca.2011.08.038

Bryant, J.A., Yogodzinski, G.M., Hall, M.L., Lewicki, J.L., Bailey, D.G., 2006. Geochemical Constraints on the Origin of Volcanic Rocks from the Andean Northern Volcanic Zone, Ecuador. J. Petrology 47, 1147–1175. doi:10.1093/petrology/egl006

Cogez, A., Meynadier, L., Allègre, C., Limmois, D., Herman, F., Gaillardet, J., 2015. Constraints on the role of tectonic and climate on erosion revealed by two time series analysis of marine cores around New Zealand. Earth and Planetary Science Letters 410, 174–185. doi:10.1016/j.epsl.2014.11.029

Condie, K.C., 1993. Chemical composition and evolution of the upper continental crust: Contrasting results from surface samples and shales. Chemical Geology 104, 1–37. doi:10.1016/0009-2541(93)90140-E

Dellinger, M., 2013. Apport des isotopes du lithium et des éléments alcalins à la compréhension des processus d'altération chimique et de recyclage sédimentaire. Institut de Physique du globe de Paris, Paris.

Dellinger, M., Bouchez, J., Gaillardet, J., Faure, L., 2015a. Testing the Steady State Assumption for the Earth's Surface Denudation Using Li Isotopes in the Amazon Basin. Procedia Earth and Planetary Science, 11th Applied Isotope Geochemistery Conference AIG-11 13, 162–168. doi:10.1016/j.proeps.2015.07.038

Dellinger, M., Gaillardet, J., Bouchez, J., Calmels, D., Galy, V., Hilton, R.G., Louvat, P., France-Lanord, C., 2014. Lithium isotopes in large rivers reveal the cannibalistic nature of modern continental weathering and erosion. Earth and Planetary Science Letters 401, 359–372. doi:10.1016/j.epsl.2014.05.061

Dellinger, M., Gaillardet, J., Bouchez, J., Calmels, D., Louvat, P., Dosseto, A., Gorge, C., Alanoca, L., Maurice, L., 2015b. Riverine Li isotope fractionation in the Amazon River basin controlled by the weathering regimes. Geochimica et Cosmochimica Acta 164, 71–93. doi:10.1016/j.gca.2015.04.042

Driver, L.A., Creaser, R.A., Chacko, T., Erdmer, P., 2000. Petrogenesis of the Cretaceous Cassiar batholith, Yukon–British Columbia, Canada: Implications for magmatism in the North

American Cordilleran Interior. Geological Society of America Bulletin 112, 1119–1133. doi:10.1130/0016-7606(2000)112<1119:POTCCB>2.0.CO;2
Gaillardet, J., Dupré, B., Allègre, C.J., 1995. A global geochemical mass budget applied to the Congo basin rivers: Erosion rates and continental crust composition. Geochimica et Cosmochimica Acta 59, 3469–3485. doi:10.1016/0016-7037(95)00230-W
Gaillardet, J., Dupre, B., Allegre, C.J., Négrel, P., 1997. Chemical and physical denudation in the Amazon River Basin. Chemical Geology 142, 141–173. doi:10.1016/S0009-2541(97)00074-0
Galy, A., France-Lanord, C., 2001. Higher erosion rates in the Himalaya: Geochemical constraints on riverine fluxes. Geology 29, 23–26. doi:http://dx.doi.org/10.1130/0091-7613(2001)0292.0.CO;2
Galy, V., France-Lanord, C., Beyssac, O., Faure, P., Kudrass, H., Palhol, F., 2007. Efficient organic carbon burial in the Bengal fan sustained by the Himalayan erosional system. Nature 450, 407–410. doi:10.1038/nature06273
Garzione, C.N., Patchett, P.J., Ross, G.M., Nelson, J., 1997. Provenance of Paleozoic sedimentary rocks in the Canadian Cordilleran miogeocline: a Nd isotopic study. Canadian Journal of Earth Sciences 34, 1603–1618.
Guyot, J.L., Fillzola, N., Quintanilla, J., Cortez, J., 1996. Dissolved solids and suspended sediment yields in the Rio Madeira basin, from the Bolivian Andes to the Amazon. IAHS PUBLICATION 55–64.
Hartmann, J., & Moosdorf, N. (2012). The new global lithological map database GLiM: A representation of rock properties at the Earth surface. Geochemistry, Geophysics, Geosystems, 13(12).
Heffernan, R.S., 2004. Temporal, geochemical, isotopic, and metallogenic studies of mid-cretaceous magmatism in the Tintina Gold Province, southeastern Yukon and southwestern Northwest Territories, Canada. University of British Columbia.
Henchiri, S., Gaillardet, J., Dellinger, M., Bouchez, J., Spencer, R.G.M., 2016. Temporal variations of riverine dissolved lithium isotopic signatures unveil contrasting weathering regimes in low-relief Central Africa. Geophys. Res. Lett. 2016GL067711. doi:10.1002/2016GL067711
Hoorn, C., Roddaz, M., Dino, R., Soares, E., Uba, C., Ochoa-Lozano, D., Mapes, R., 2009. The Amazonian Craton and its Influence on Past Fluvial Systems (Mesozoic-Cenozoic, Amazonia), in: Hoorn, C., Wesselingh, F.P. (Eds.), Amazonia: Landscape and Species Evolution. Wiley-Blackwell Publishing Ltd., pp. 101–122.
Lupker, M., France-Lanord, C., Galy, V., Lavé, J., Gaillardet, J., Gajurel, A.P., Guilmette, C., Rahman, M., Singh, S.K., Sinha, R., 2012. Predominant floodplain over mountain weathering of Himalayan sediments (Ganga basin). Geochimica et Cosmochimica Acta 84, 410–432. doi:10.1016/j.gca.2012.02.001
Lupker, M., France-Lanord, C., Galy, V., Lavé, J., Kudrass, H., 2013. Increasing chemical weathering in the Himalayan system since the Last Glacial Maximum. Earth and Planetary Science Letters 365, 243–252. doi:10.1016/j.epsl.2013.01.038
Lupker, M., France-Lanord, C., Lavé, J., Bouchez, J., Galy, V., Métivier, F., Gaillardet, J., Lartiges, B., Mugnier, J.-L., 2011. A Rouse-based method to integrate the chemical composition of river sediments: Application to the Ganga basin. J. Geophys. Res. 116, F04012. doi:10.1029/2010JF001947
McLennan, S.M., 1993. Weathering and Global Denudation. The Journal of Geology 101, 295–303.

Meade, R.H., 1985. Suspended sediment in the Amazon River and its tributaries in Brazil during 1982-84 (USGS Numbered Series No. 85-492), Open-File Report. U.S. Geological Survey,.

Miskovic, A., 2008. Magmatic evolution of the Peruvian Eastern Cordilleran intrusive belt: insights into the growth of continental crust and tectonism along the proto-Andean Western Gondwana. University of Geneva.

Moquet, J.-S., Crave, A., Viers, J., Seyler, P., Armijos, E., Bourrel, L., Chavarri, E., Lagane, C., Laraque, A., Casimiro, W.S.L., Pombosa, R., Noriega, L., Vera, A., Guyot, J.-L., 2011. Chemical weathering and atmospheric/soil CO2 uptake in the Andean and Foreland Amazon basins. Chemical Geology 287, 1–26. doi:10.1016/j.chemgeo.2011.01.005

Morrow, D.W., 1999. Lower Paleozoic stratigraphy of northern Yukon Territory and northwestern District of Mackenzie (No. 538).

Petford, N., Atherton, M., 1996. Na-rich Partial Melts from Newly Underplated Basaltic Crust: the Cordillera Blanca Batholith, Peru. J. Petrology 37, 1491–1521. doi:10.1093/petrology/37.6.1491

Pinto, L. del C., 2003. Traçage de l'érosion cénézoïque des Andes centrales à l'aide de la minéralogie et géochimie des sédiments (Nord du Chili et Nord-Ouest de la Bolivie) (Thèse doctorat). Universidad de Chile. Departamento de geologia, France.

Reeder, S.W., Hitchon, B., Levinson, A.A., 1972. Hydrogeochemistry of the surface waters of the Mackenzie River drainage basin, Canada—I. Factors controlling inorganic composition. Geochimica et Cosmochimica Acta 36, 825–865. doi:10.1016/0016-7037(72)90053-1

Roddaz, M., Viers, J., Brusset, S., Baby, P., Hérail, G., 2005. Sediment provenances and drainage evolution of the Neogene Amazonian foreland basin. Earth and Planetary Science Letters 239, 57–78. doi:10.1016/j.epsl.2005.08.007

Ross, D.J.K., Bustin, R.M., 2009. Investigating the use of sedimentary geochemical proxies for paleoenvironment interpretation of thermally mature organic-rich strata: Examples from the Devonian–Mississippian shales, Western Canadian Sedimentary Basin. Chemical Geology 260, 1–19. doi:10.1016/j.chemgeo.2008.10.027

Rudnick, R.L., Gao, S., 2014. 4.1 - Composition of the Continental Crust, in: Turekian, H.D.H.K. (Ed.), Treatise on Geochemistry (Second Edition). Elsevier, Oxford, pp. 1–51.

Santos, J.O.S., Hartmann, L.A., Gaudette, H.E., Groves, D.I., Mcnaughton, N.J., Fletcher, I.R., 2000. A new understanding of the provinces of the Amazon Craton based on integration of field mapping and U-Pb and Sm-Nd geochronology. Gondwana Research 3, 453–488.

Singh, S.K., France-Lanord, C., 2002. Tracing the distribution of erosion in the Brahmaputra watershed from isotopic compositions of stream sediments. Earth and Planetary Science Letters 202, 645–662. doi:10.1016/S0012-821X(02)00822-1

Singh, S.K., Rai, S.K., Krishnaswami, S., 2008. Sr and Nd isotopes in river sediments from the Ganga Basin: Sediment provenance and spatial variability in physical erosion. J. Geophys. Res. 113, F03006. doi:10.1029/2007JF000909

Viers, J., Roddaz, M., Filizola, N., Guyot, J.-L., Sondag, F., Brunet, P., Zouiten, C., Boucayrand, C., Martin, F., Boaventura, G.R., 2008. Seasonal and provenance controls on Nd–Sr isotopic compositions of Amazon rivers suspended sediments and implications for Nd and Sr fluxes exported to the Atlantic Ocean. Earth and Planetary Science Letters 274, 511–523. doi:10.1016/j.epsl.2008.08.011

Wang, Q.-L., Chetelat, B., Zhao, Z.-Q., Ding, H., Li, S.-L., Wang, B.-L., Li, J., Liu, X.-L., 2015. Behavior of lithium isotopes in the Changjiang River system: Sources effects and response to weathering and erosion. Geochimica et Cosmochimica Acta 151, 117–132.

doi:10.1016/j.gca.2014.12.015
Wittmann, H., Blanckenburg, F. von, Maurice, L., Guyot, J.-L., Filizola, N., Kubik, P.W., 2010. Sediment production and delivery in the Amazon River basin quantified by in situ—produced cosmogenic nuclides and recent river loads. Geological Society of America Bulletin B30317.1. doi:10.1130/B30317.1

Supplemental Table

Click here to download Supplemental file Table-DR1 - Geology - Accepted.xlsx

Sample name	Basin	River	Location	Longitude	Latitude	References for Li isotope data	Surface	Discharge	D_{90}	Al	Li	$^{143}Nd/^{144}Nd$	$\varepsilon_{Nd}(0)$	δ^7Li	Li/Al ($\times10^{-3}$)	CIA	$[Li]_{diss}$
							(km^2)	(m^3/s)	(μm)	($\mu g/g$)	($\mu g/g$)			(‰)	(g/g)		(mmol/L)
Amazon Lowlands																	
AM01-17	Amazon	Orthon	Riberalta	66°02'11,0" W	10°48'39,9" S	Dellinger et al., (2014, 2015)	33485	475		89835	59	0.512158	-9.37	-5.7	0.66	82	0.31
AM01-18	Amazon	Yata	Mouth	65°35'00,2" W	10°58'44,8" S	Dellinger et al., (2014, 2015)	20770	222		115390	100	0.512043	-11.61	-5.3	0.87	86	0.08
AM01-27	Amazon	Trombetas	Mouth	N.D.	N.D.	Dellinger et al., (2014, 2015)	250000	6200		115312	20	0.511609	-20.08	-5.1	0.17	92	0.037
AM01-22 MES	Amazon	Negro	Paricatuba	N.D.	N.D.	Dellinger et al., (2014, 2015)	691000	29000		113016	44	0.511930	-13.81	-2.7	0.39	87	0.031
AM6/1-09 MES	Amazon	Urucara	Mouth	N.D.	N.D.	Dellinger et al., (2014, 2015)	150000	3000		110691	43	0.511895	-14.50	-4.0	0.39	87	0.049
AM01-29	Amazon	Tapajos	Mouth	N.D.	N.D.	Dellinger et al., (2014, 2015)	490000	13500		129350	27	0.511698	-18.33	-6.0	0.20	93	0.038
Congo																	
C89-63 PK 1105	Congo	Congo	Mouth	N.D.	N.D.	Henchiri et al., (2016), this study	3700000	38026			29	0.511796	-16.43	-6.2			0.10
C89-65 PK 1105	Congo	Congo	Mouth	N.D.	N.D.	Henchiri et al., (2016), this study	3700000	38026		117769	23	0.511833	-15.70	-5.1	0.19	92	0.10
Amazon Andes																	
AM01_08	Amazon	Alto Beni	Mouth	67°40'18' W	15°07'24" S	Dellinger et al., (2014, 2015)	21197	750		84800	79	0.512011	-12.24	-1.8	0.93	74	1.62
AM07_04	Amazon	Beni	Rurrenabaque	67°32'05,2" W	14°28'26,8" S	Dellinger et al., (2014, 2015)	69980	2153	44	95289	87	0.511998	-12.49	-3.1	0.91	76	1.28
AM07_09	Amazon	Beni	Riberalta	66°05'53,8" W	10°58'44,8" S	Dellinger et al., (2014, 2015)	114379	3772	50	83319	78	0.511994	-12.56	-2.9	0.94	76	0.57
AM05_19	Amazon	Madeira	Foz Madeira	58°48'30,1" W	03°27'00,9" S	Dellinger et al., (2014, 2015)	1325000	31250	36	111822	99	0.512097	-10.55	-3.4	0.89	78	0.18
AM06_65	Amazon	Amazonas	Obidos	55°30'18,6" W	01°56'05,3" S	Dellinger et al., (2014, 2015)	4618750	182200	27	107370	81	0.512141	-9.70	-3.6	0.75	78	0.14
AM08_13	Amazon	Ucayali	Jenaro Herrera	73°40'28" W	04°54'28" S	Dellinger et al., (2014, 2015)	352593	12090	50	85664	58	0.512158	-9.37	-1.9	0.73	68	0.66
AM06_14	Amazon	Solimoes	Manacapuru	60°33'11,0" W	03°19'41,0" S	Dellinger et al., (2014, 2015)	2148000	103000	35	100535	58	0.512101	-10.48	-2.6	0.58	76	0.14
AM08_36	Amazon	Pastaza	Embouchure	N.D.	N.D.	Dellinger et al., (2014, 2015)	39000	2770	61	97031	26	0.512512	-2.45	-0.2	0.27	68	0.14
AM07_14	Amazon	Madre de Dios	Riberalta	66°05'54" W	10°57'46" S	Dellinger et al., (2014, 2015)	124231	5602	35	94447	75	0.512106	-10.38		0.79	77	0.22
Mackenzie																	
CAN09_51	Mackenzie	Red Arctic	Tsiigehtchic	133°46'44.3" W	67°25'34.2" N	Dellinger et al., (2014)	18600	159	23	79022	78.1	0.512066	-11.16	-2.4	0.99	77	0.89
CAN09_04	Mackenzie	Liard	Fort_Simpson	121°17'6.2" W	61°50'8.6" N	Dellinger et al., (2014)	275000	2450	49	64955	51.2	0.511904	-14.31	-1.7	0.79	73	0.63
CAN09_47	Mackenzie	Mackenzie	Tsiigehtchic	133°43'23.8" W	67°27'30.1" N	Dellinger et al., (2014)	1680000	8990		76477	67.5	0.512013	-12.19	-1.9	0.88	76	0.57
CAN10_32	Mackenzie	Middle Channel	Inuvik	134°4'49.8" W	68°24'33.3" N	Dellinger et al., (2014)	1805200		14	90608	79.3	0.511979	-12.86	-1.7	0.88	79	
CAN09_40	Mackenzie	Peel	Fort_McPherson	134°52'8.6" W	68°19'56.6" N	Dellinger et al., (2014)	70600	686	18	80981	81.5	0.512062	-11.23	-2.1	1.01	77	0.71
CAN09_28	Mackenzie	Slave	Fort_Smith	111°53'25.7" W	60°0'59.5" N	Dellinger et al., (2014)	616400	3200	17	77069	52.8	0.512014	-12.18	-1.3	0.68	76	0.60
Changjiang																	
CJ1	Changjiang	Jinshajiang	Panzhihua	101°37.551' E	26°34.503' N	Wang et al., (2015)	285556	1309	24	80546	48.5			-2.2	0.60	69	2.07
CJ4	Changjiang	Jinshajiang	Yibin	104°33.385' E	28°42.164' N	Wang et al., (2015)	485000	8239	22	82252	48.7			-0.5	0.59	73	0.97
CJ14	Changjiang	Changjiang	Chongqing	N.D.	N.D.	Wang et al., (2015)	867000	10945	24	84970	53.8			-1.0	0.63	71	0.78
CJ60	Changjiang	Changjiang	Yueyang	113°18.739' E	29°38.079' N	Wang et al., (2015)	1250000	15844			76.6			-1.3			0.37
CJ52	Changjiang	Changjiang	Wuhan	114°29.876' E	30°40.747' N	Wang et al., (2015)	1488000	22340	45	83606	61.9			-1.6	0.74	72	0.44
CJ36	Changjiang	Changjiang	Datong	117°38.324' E	30°46.085' N	Wang et al., (2015)	1705000	28266	26	98071	70.9			-1.7	0.72	76	0.27
CJ2	Changjiang	Yalongjiang	Panzhihua	101°49.200' E	26°40.127' N	Wang et al., (2015)	128444	1857		161917	41.3			0.1	0.26	63	0.68
CJ5	Changjiang	Minjiang	Yibin	104°33.721' E	28°48.779' N	Wang et al., (2015)	133000	2732	33	83956	67.0			0.0	0.80	67	0.45
CJ33	Changjiang	Xiangjiang	Changsha	112°56.795' E	28°07.364' N	Wang et al., (2015)	94700	2405	15	108398	86.7			-3.4	0.80	82	0.16
CJ34	Changjiang	Ganjiang	Nanchang	115°52.053' E	28°40.206' N	Wang et al., (2015)	80900	2104		103092	88.6			-4.7	0.86	80	0.25
Ganges-Brahmaputra																	
IND99-19 MES	Ganges	Ganga	Harding bridge	89°1'28.739" E	24°3'10.44" N	Dellinger et al., (2014)	1050000	15622		94322	55.0	0.511725	-17.81	-1.02	0.58		0.49
BR8210	Brahmaputra	Brahmaputra	Jamuna bg.	N.D.	N.D.	Dellinger et al., (2014)	580000	16161		87063	47	0.511897	-14.45	-1.38	0.54	66	1.08
Western cordillera																	
CAN99-28 MES	Skeena	Skeena	Kitwanga	N.D.	N.D.	This study	42200	962		83647	28.7			2.0	0.34	64	0.05
CAN99-39 MES	Stikine	Stikine	Iskut	N.D.	N.D.	This study	29300	755		75071	24.5			1.2	0.33	63	0.10

TDS_{Sil}	Sample name	River	Cation silicate Weathering rate	Total silicate Weathering rate (W)	Sediment concentration	Erosion rate (E)	Denudation rate (D)	Weathering Intensity (W/D)	Proportion of shales	δ^7Li_{rock}	$\Delta^7Li_{sed-rock}$	$1-w^{Li}$	$(Li/Al)_{sed}$ / $(Li/Al)_{rock}$
(mg/L)			(t/km^2/yr)	(t/km^2/yr)	(mg/L)	(t/km^2/yr)	(t/km^2/yr)			(‰)	(‰)		
	Amazon Lowlands												
19.6	AM01-17	Orthon	2.8	8.8	123	55	64	0.137	0.73 ± 0.12	-0.10 ± 0.89	-5.58 ± 1.07	0.77 ± 0.09	0.83 ± 0.11
10.4	AM01-18	Yata	0.8	3.5	30	10	14	0.259	0.95 ± 0.14	-0.36 ± 0.93	-4.90 ± 1.12	0.84 ± 0.07	0.91 ± 0.12
7.8	AM01-27	Trombetas		6.1	8	6	12	0.504	0.00 ± 0.10	3.50 ± 1.50	-8.63 ± 1.75	0.38 ± 0.14	0.58 ± 0.10
4.3	AM01-22 MES	Negro		5.7	10	14	20	0.291	0.73 ± 0.10	-0.11 ± 0.90	-2.61 ± 1.20	0.68 ± 0.15	0.49 ± 0.07
8.7	AM6/1-09 MES	Urucara		5.5	15	10	15	0.367	0.65 ± 0.11	0.04 ± 0.90	-4.02 ± 1.10	0.66 ± 0.12	0.52 ± 0.08
11.5	AM01-29	Tapajos		10.0	8	7	17	0.581	0.28 ± 0.14	1.37 ± 1.11	-7.37 ± 1.50	0.45 ± 0.18	0.42 ± 0.20
	Congo												
15.0	C89-63 PK 1105	Congo		5.3	25	8.1	13	0.396	0.35 ± 0.10			0.51 ± 0.13	
15.0	C89-65 PK 1105	Congo		5.3	25	8.1	13	0.396	0.48 ± 0.11	1.00 ± 1.11	-6.05 ± 1.20	0.45 ± 0.12	0.31 ± 0.07
	Amazon Andes												
26.4	AM01_08	Alto Beni	20.5	29.5	3403	3800	3829	0.008	1.00 ± 0.10	-0.50 ± 1.00	-1.26 ± 1.00		
17.4	AM07_04	Beni	8.9	16.9	3234	3140	3157	0.005	1.00 ± 0.10	-0.50 ± 1.00	-2.59 ± 1.12	0.97 ± 0.03	0.91 ± 0.08
14.9	AM07_09	Beni	5.8	15.5	980	1020	1036	0.015	1.00 ± 0.10	-0.50 ± 1.00	-2.38 ± 1.12	0.95 ± 0.03	0.94 ± 0.08
12.8	AM05_19	Madeira	3.2	9.5	248	184	194	0.049	0.85 ± 0.12	-0.30 ± 1.00	-3.08 ± 1.10	0.95 ± 0.03	0.98 ± 0.12
11.4	AM06_65	Amazonas		14.2	186	231	245	0.058	0.76 ± 0.12	-0.15 ± 1.00	-3.43 ± 1.09	0.94 ± 0.03	0.92 ± 0.12
15.6	AM08_13	Ucayali	8.5	16.9	527	570	587	0.029	0.70 ± 0.08	-0.10 ± 0.89	-1.80 ± 1.05	0.87 ± 0.06	0.92 ± 0.10
13.1	AM06_14	Solimoes		19.8	124	188	207	0.096	0.80 ± 0.12	-0.24 ± 0.96	-2.36 ± 1.10	0.88 ± 0.06	0.69 ± 0.15
24.2	AM08_36	Pastaza	31.7	54.3					0.32 ± 0.10	1.10 ± 0.93	-1.28 ± 1.14		
14.6	AM07_14	Madre de Dios	7.5	20.7	401	570	591	0.035	0.82 ± 0.10			0.95 ± 0.03	0.92 ± 0.10
	Mackenzie												
8.0	CAN09_51	Red Arctic	1.37	2.2	1454	392	395	0.005	0.95 ± 0.10	-0.47 ± 0.91	-1.94 ± 1.10	0.95 ± 0.03	1.04 ± 0.10
8.7	CAN09_04	Liard	1.19	2.4	595	167	170	0.014	0.75 ± 0.10	-0.04 ± 0.91	-1.62 ± 1.08	0.87 ± 0.06	0.97 ± 0.12
9.5	CAN09_47	Mackenzie	1.03	1.6	377	64	65	0.025	0.80 ± 0.10	-0.20 ± 0.91	-1.72 ± 1.08	0.87 ± 0.06	1.00 ± 0.12
	CAN10_32	Middle Channel							0.70 ± 0.10	-0.04 ± 0.91	-1.65 ± 1.05		1.10 ± 0.12
8.8	CAN09_40	Peel	1.73	2.7	961	295	297	0.009	1.00 ± 0.10	-0.50 ± 0.91	-1.56 ± 1.10	0.94 ± 0.03	1.01 ± 0.10
12.0	CAN09_28	Slave	1.14	2.0	348	57	59	0.033	0.65 ± 0.10	0.15 ± 0.91	-1.45 ± 1.07	0.82 ± 0.08	0.92 ± 0.14
	Changjiang												
18.6	CJ1	Jinshajiang	1.4	2.7	1211	175	178	0.015	0.50 ± 0.15	0.82 ± 1.13	-3.02 ± 1.26	0.80 ± 0.088	
18.5	CJ4	Jinshajiang	4.8	9.9	538	289	299	0.033	0.50 ± 0.15	0.78 ± 1.16	-1.28 ± 1.20	0.79 ± 0.088	
13.4	CJ14	Changjiang	1.7	5.4	1226	488	494	0.011	0.58 ± 0.15	0.48 ± 1.03	-1.48 ± 1.20	0.92 ± 0.04	
14.2	CJ60	Changjiang	1.8	5.7	740	296	302	0.019	0.84 ± 0.15	0.49 ± 1.02	-1.79 ± 1.13	0.96 ± 0.03	
16.9	CJ52	Changjiang	3.3	8.0	572	271	279	0.029	0.68 ± 0.15	-0.31 ± 0.99	-1.29 ± 1.11	0.92 ± 0.04	
16.7	CJ36	Changjiang	2.4	8.7	475	249	257	0.034	0.78 ± 0.15	-0.18 ± 0.99	-1.52 ± 1.10	0.95 ± 0.03	
17.0	CJ2	Yalongjiang	3.1	7.8	205	93	101	0.077	0.38 ± 0.15	1.40 ± 1.20	-1.30 ± 1.63	0.64 ± 0.117	
18.3	CJ5	Minjiang	7.1	11.9	552	358	370	0.032	0.74 ± 0.15	-0.07 ± 0.97	0.07 ± 1.09	0.92 ± 0.04	
13.3	CJ33	Xiangjiang	1.7	10.6	153	122	133	0.080	0.92 ± 0.15	-0.36 ± 0.93	-3.04 ± 1.10	0.92 ± 0.04	
22.4	CJ34	Ganjiang	3.2	18.4	169	138	157	0.117	1.00 ± 0.15	-0.50 ± 1.00	-4.20 ± 1.20	0.90 ± 0.055	
	Ganges-Brahmaputra												
29.8	IND99-19 MES	Ganga		14	1129	530	544	0.026	0.30 ± 0.10	-0.40 ± 0.95	-0.62 ± 1.00	0.95 ± 0.029	0.99 ± 0.15
11.8	BR8210	Brahmaputra		10	921	810	820	0.013	0.20 ± 0.10	0.33 ± 1.10	-1.71 ± 1.30	0.85 ± 0.069	1.02 ± 0.12
	Western cordillera												
7.9	CAN99-28 MES	Skeena	4.2	5.7	362	261	266	0.021	0.00 ± 0.10	3.50 ± 1.10	-1.45 ± 1.00	0.97 ± 0.03	1.02 ± 0.10
7.2	CAN99-39 MES	Stikine	4.1	5.9	755	614	620	0.009	0.10 ± 0.10	2.06 ± 1.20	-0.86 ± 1.00	0.96 ± 0.03	0.86 ± 0.10